Interner Bericht

DLR-IB-AE-GO-2024-103

Set-up of a generic, aeroelastic simulation model for demonstration and software testing purposes

Master Thesis

Francisco Carvalho

Deutsches Zentrum für Luft- und Raumfahrt

Institute of Aeroelasticity
Göttingen

Deutsches Zentrum
für Luft- und Raumfahrt

Document Properties

Title	Set-up of a generic, aeroelastic simulation model for demonstration and software testing purposes	
Subject	Master Thesis	
Institute	Institute of Aeroelasticity	
Compiled by	Francisco Manuel Carneiro Pinto Branco Carvalho	Francisco Carvalho
Participants		
Checked by	Dr. -Ing. Arne Voß	Arne Voß Digital signiert von Arne Voß DN: PostalCode=51147, O=Deutsches Zentrum fuer Luft- und Raumfahrt e. V. (DLR), STREET=Linder Höhe, S= Nordrhein-Westfalen, C=DE, CN=Arne Voß, E= arne.voss@dlr.de Grund: Ich habe dieses Dokument geprüft Ort: Göttingen Datum: 2024.07.04 15:07:19+02'00' Foxit PDF Reader Version: 2024.2.2
Release by	Prof. Dr. -Ing. Wolf Reiner Krüger	W. Krüger Digital signiert von Wolf-Reiner Krueger DN: C=DE, O=Deutsches Zentrum fuer Luft- und Raumfahrt e.V. (DLR), SN=Krueger, G=Wolf-Reiner, CN=Wolf-Reiner Krueger Grund: Ich genehmige dieses Dokument Ort: Göttingen Datum: 2024.07.04 15:25:17+02'00' Foxit PDF Editor Version: 13.1.2
Date	07. July 2024	
Version	1.0	
File Path		

DEGREE PROJECT IN TECHNOLOGY,
SECOND CYCLE, 30 CREDITS
STOCKHOLM, SWEDEN 2024

Deutsches Zentrum
für Luft- und Raumfahrt
German Aerospace Center

Set-up of a generic aeroelastic simulation model for demonstration and software testing purposes

FRANCISCO CARVALHO

KTH ROYAL INSTITUTE OF TECHNOLOGY
SCI SCHOOL OF ENGINEERING SCIENCES

DLR - Deutsches Zentrum für Luft- und Raumfahrt
German Aerospace Center

Authors

Francisco Carvalho - fracar@kth.se
Aerospace Engineering
KTH Royal Institute of Technology

Place of Project

Göttingen, Germany
DLR - Institute of Aeroelasticity

Examiner

Raffaello Mariani
Stockholm, Sweden
KTH Royal Institute of Technology

Supervisors

Raffello Mariani

Stockholm, Sweden

KTH Royal Institute of Technology

Arne Voß

Göttingen, Germany

DLR - Institute of Aeroelasticity

Abstract

This thesis presents the development and comprehensive analysis of an open-source aeroelastic model for the Douglas DC-3 with some modifications. The model serves as a platform for software testing, capturing essential aeroelastic phenomena. It features a conventional configuration with two engines, control surfaces, and a wing with a leading-edge sweep angle of 15.5°, dihedral angle of 5°, aspect ratio of 9.2, and cambered airfoil, operating in a subsonic regime.

The development process included finite element modeling using beam elements, aerodynamic modeling with the Doublet Lattice Method (DLM), and mass modeling, including a complex fuel mass model. Four distinct mass configurations were analyzed. Trim case analyses were performed using both *Loads Kernel* and SOL144 in *MSC Nastran*, revealing significant differences between rigid and flexible configurations. Maneuver load analyses were conducted exclusively using *Loads Kernel*.

Additionally, gust loads were studied using the (1-cos) Discrete Gust Model, demonstrating coupling with the short-period mode due to high static margin. Flutter checks showed matching results between *Loads Kernel* and *MSC Nastran*, with flutter speeds of 195 m/s and 203 m/s, respectively, confirming the model's plausibility for aeroelastic analysis.

Keywords

Aeroelasticity, Douglas DC-3, Finite Element Modeling, Doublet Lattice Method, Trim Analysis, Maneuver Loads, Gust Loads, Flutter Analysis

Abstract

Denna avhandling presenterar utvecklingen och en omfattande analys av en öppen källkods aeroelastisk modell för Douglas DC-3 med vissa modifieringar. Modellen fungerar som en plattform för programvarutestning och fångar viktiga aeroelastiska fenomen. Den har en konventionell konfiguration med två motorer, styrytor och en vinge med en framkantssvepvinkel på 15,5°, en dihedralvinkel på 5°, ett aspektförhållande på 9,2 och en välvd vingprofil, som opererar i ett subsoniskt regime.

Utvecklingsprocessen inkluderade finita element-modellering med balkelement, aerodynamisk modellering med Doublet Lattice Method (DLM) och massmodellering, inklusive en komplex bränslemassmodell. Fyra distinkta masskonfigurationer analyserades. Trimsituationer analyserades med både *Loads Kernel* och SOL144 i *MSC Nastran*, vilket avslöjade betydande skillnader mellan stela och flexibla konfigurationer. Manöverlastanalyser genomfördes exklusivt med *Loads Kernel*.

Dessutom studerades vindbybelastningar med (1-cos) Diskret Gustmodell, vilket visade koppling med kortperiodläget på grund av hög statisk marginal. Fladdertester visade matchande resultat mellan *Loads Kernel* och *MSC Nastran*, med fladderhastigheter på 195 m/s respektive 203 m/s, vilket bekräftade modellens tillförlitlighet för aeroelastisk analys.

Nyckelord

Aeroelasticitet, Douglas DC-3, Finite Element Modeling, Doublet Lattice Method, Trimsituationanalys, Manöverbelastningar, Vindbybelastningar, Fladdertester

Nomenclature

Abbreviations

3AS	Active Aeroelastic Aircraft Structures
AePW	Aeroelastic Prediction Workshop
BSCW	Benchmark Supercritical Wing
CRM	Common Research Model
DLM	Doublet-Lattice Method
DLR	Deutsche Zentrum für Luft- und Raumfahrt
EC	European Comission
FEA	Finite Element Analyses
FEM	Finite Element Model
HT	Horizontal Tail
LE	Leading Edge
LRA	Load Reference Axis
TE	Trailing Edge
USAF	Air Force Flight Dynamics Laboratory
VT	Vertical Tail

Variables and Parameters

Latin

A	Area of cross section	m^2
AR	Aspect ratio	
b	Wingspan	m
$\overline{c}$	Mean aerodynamic chord	m
Cg	Center of gravity	m
C_L	Lift coefficient	
$C_{L_{cs}}$	Lift coefficient due to control surface deflection	
C_{L_f}	Lift coefficient due to elastic deformation	
E	Young’s modulus	Pa
EAS	Equivalent airspeed	m/s
F	Flutter matrix	
F_g	Flight profile alleviation factor	
F_z	Shear force	N
f	Frequency	Hz
f_a	Aerodynamic forces	N
G	Shear modulus	Pa
H	Gust gradient	m
h	Aircraft height	m
$I1$	Area of moment of inertia about axis 1	m^4
$I2$	Area of moment of inertia about axis 2	m^4
I_{ji}	Mass moments of inertia	$kg\ m^2$
J	Torsional constant	m^4
K	Stiffness matrix	
l	Aircraft length	m
M	Mass matrix	
Ma	Mach number	
$MTOM$	Maximum take-off mass	kg

M_x	Bending moment	*Nm*
M_y	Torsional moment	*Nm*
m	Mass	*kg*
m_{ht}	Horizontal mass	*kg*
m_{vt}	Vertical mass	*kg*
m_{wing}	Wing mass	*kg*
n_Z	Load factor	
OEM	Operational empty mass	*kg*
P/M	Power/mass	*W/kg*
p	Laplace variable	
p	Roll velocity	*rad/s*
Q	Aerodynamic transfer matrix	
q	Dynamic pressure	*Pa*
R	Range	*km*
ROC	Rate of climb	*m/s*
S	Wing area	m^2
TAS	True airspeed	*m/s*
t/c	Thickness-to-chord ratio	
t_{skin}	Skin thickness	*m*
t_{spar}	Spar thickness	*m*
t_{str}	Stringers thickness	*m*
t_{ws}	Wing skin thickness	*m*
U_{ds}	Design gust velocity	*m/s*
U_{ref}	Reference gust velocity	*m/s*
V_A	Maneuvering speed	*m/s*
V_B	Design speed for maximum gust intensity	*m/s*
V_C	Cruise speed	*m/s*
V_D	Diving speed	*m/s*
$V_{flutter}$	Flutter speed	*m/s*

V_{NE}	Never exceed speed	m/s
V_S	Stall speed	m/s
v	Displacement vector	m
W_e	Empty aircraft weight	kg
W/S	Wing loading	kg/m^2

Greek

α_i	Incidence angle	*degree or rad*
α_{trim}	Trim angle of attack	*degree or rad*
Γ	Dihedral angle	*degree or rad*
γ	Poisson's ratio	
η_{trim}	Trim elevator deflection	*degree or rad*
Λ_{LE}	Sweep of the leading edge	*degree or rad*
ρ	Mass density	kg/m^3
Φ	Washin/washout angle	*degree or rad*

Contents

Chapter 1

Introduction

1.1 Motivation

The sparseness of open-source generic aeroelastic simulation models poses a significant challenge, as existing options are invariably held back by limitations. It is imperative, particularly for purposes of demonstration and software testing, to ensure the availability of a generic model that encompasses the essential components of an aircraft, striking a wise balance between simplicity and fidelity to reality.

One illustrative instance of an open-source structural finite element model of a generic aircraft configuration is FERMAT, as documented in [21]. The geometric foundation of FERMAT is rooted in the NASA Common Research Model (CRM) [30], similar in size and overall parameters to a long-range wide-body transport aircraft configuration. Notwithstanding its relevance, the CRM's design for Ma=0.85 flight introduces complexities, particularly in the transonic regime, where unsteady aerodynamic phenomena, such as shock-induced separation effects, cause nonlinearities and potentially influence flutter boundaries, making it less than ideal for demonstration purposes. Furthermore, it is impossible to tune in some properties or exaggerate some effects to highlight flexibility or flutter mechanism for example.

In parallel, the Active Aeroelastic Aircraft Structures (3AS) project [31], funded by the European Comission (EC), extensively explored active aeroelastic concepts for a group of different classes of reference aircraft: a 4-engine wide body transport aircraft, designated as the EuRAM [22] configuration; a commuter jet aircraft, designated as the X-DIA [29]; and a high aspect ratio – high altitude configuration (HARW)

[18]. Regrettably, while the project presented a range of aircraft models, they were exclusively disseminated among project partners, preventing public access to aeroelastic models.

Another open-source aircraft model, integral to the Aeroelastic Prediction Workshop (AePW) [17], emphasizes the evaluation of existing computer codes and modeling techniques. As well, one of the workshop's goal is to identify computational and experimental areas needing additional research and development. The chosen configuration for the workshop, Benchmark Supercritical Wing (BSCW), however, provides only the wing model, and not the entirety of an aircraft model.

Motivated by this noticable absence of an open-source generic aeroelastic model possessing required complexity, the aeroelastic model of the Douglas DC-3 has been meticulously established. This model serves as a demonstrative platform for software testing, including Deutsche Zentrum für Luft- und Raumfahrt (DLR) in-house tool the *Loads Kernel* Software [34] and the commercial software *MSC Nastran* [23]. The *Loads Kernel* Software facilitates the calculation of quasi-steady and dynamic maneuver loads, unsteady gust loads in both time and frequency domains, and dynamic landing loads based on a generic landing gear module. *MSC Nastran*, a Finite Element Analyses (FEA) software, is employed for simulating and analyzing the behavior of structures and mechanical components in engineering applications.

The development of the Douglas DC-3 aeroelastic model addresses the critical knowledge gap by providing a representative and comprehensive model for demonstration and testing purposes. The overall objective is to offer a valuable resource to the broader community, serving as an example and starting point for further developments in this domain. Moreover, this work underscores the pivotal role of Aeroelasticity in Aircraft Design, Performance, and Flight Dynamics and Stability, elucidating the nuanced interplay between unsteady flow and flexible structures and emphasizing disparities between rigid and flexible aircraft approaches, highlighting aeroelastic phenomena like flutter mechanism, and the resultant variations in experienced loads.

1.2 Thesis Scope and Outline

Chapter Two aims to provide a theoretical background on finite element modeling, mass modeling, aerodynamic modeling, eigenmodes, flight trim, maneuver and gust load analyses, and aeroelastic phenomena analyses, particularly focusing on flutter. Chapter Three outlines the requirements that the aircraft model needs to fulfill. These requirements include a simple and conventional aircraft configuration, a wing featuring sweep and dihedral, control surfaces, a maximum of two engines, and operation in the subsonic regime ($\boldsymbol{Ma} > 0.6$). Additionally, the aircraft must have a representative and easily recognizable design, with extensive publicly accessible data. It should exhibit notable wing bending and torsion during level flight, with an evident flutter mechanism where bending and torsion modes are coupled. The chapter concludes with the selection of the Douglas DC-3 as the subject aircraft. Chapter Four describes and presents the aeroelastic model, encompassing the finite element model, aerodynamic model, mass model, and fuel model. It also details the different mass configurations and various modified models. Finally, the eigenmodes of the final modified model are analyzed. In Chapter Five, various analyses are performed to compare and demonstrate the capabilities of both *Loads Kernel* and *MSC Nastran*. These analyses include trim analyses, maneuver and gust load analyses, and flutter checks. The final chapter draws conclusions on the achieved aeroelastic model and the results obtained.

Chapter 2

Theoretical Background

Building on the motivation outlined in Chapter One, the following sections aim to establish a comprehensive understanding of finite element modeling, mass modeling aerodynamic modeling, eigenmodes, flight trim, maneuver and gust load analyses, and aeroelastic phenomena analyses, particularly flutter.

2.1 Finite Element Model

The Finite Element Method (FEM) is a numerical technique used to solve complex physical problems by breaking down a large system into smaller, simpler parts called finite elements. These elements are interconnected at points called nodes, and the physical properties and governing equations are applied to these elements. FEM transforms a continuous problem (such as a structural deformation) into a discrete problem that can be solved computationally [28].

In aeroelasticity, FEM is crucial for structural analyses because it allows to accurately model and predict the interaction between aerodynamic forces and structural responses. Aircraft are subjected to complex, dynamic loads, and FEM helps in understanding how these structures will deform, vibrate, or potentially fail under various flight conditions. This ensures safety, performance, and reliability in the design and operation of aerospace vehicles. It is crucial to point out that in aeroelasticity the main interest is overall structural deformations, rather than for example local stress peaks.

In the finite element modeling of the aircraft, both shell and beam elements are typically considered for the structural representation. Ultimately, beam elements were chosen primarily due to their simplicity and ease of modifying wing properties to observe various aeroelastic phenomena. Beam elements are computationally simpler and require fewer degrees of freedom compared to shell elements, making them more straightforward to implement and analyze. Additionally, it is easier to change the properties of the wing, such as stiffness and mass distribution, facilitating the study of aeroelastic effects like flutter and divergence. Beam elements also require less computational power and memory, allowing for quicker simulations, especially beneficial for preliminary design and iterative studies [12].

However, beam elements have some disadvantages. They may not capture the detailed stress distribution and deformation accurately for complex wing geometries or highly detailed stress analysis. Shell elements are more appropriate for thin-walled structures where bending and membrane effects are significant.

Beam theory simplifies the structure into one-dimensional elements that capture the bending, shear, and torsional responses. The primary assumptions in using beam elements include the Euler-Bernoulli assumption, where cross-sections of the beam remain plane and perpendicular to the neutral axis after deformation, which is valid for long, slender beams (high aspect ratio wings) where shear deformations are negligible. The material behavior is assumed to be linear elastic, implying that the stress-strain relationship is linear and follows Hooke's Law (the assumption of linear elasticity is valid for 12-15% of tip vertical displacement in relation with half wingspan). The beam elements are assumed to have a uniform cross-section along their length, which simplifies the analysis but may not be accurate for tapered or variable cross-section structures. The deformations are assumed to be small, allowing linearization of the governing equations, which might not be valid for large deflections [7, 8].

At the end, the need for a simpler, more manageable model that facilitates property modifications and aeroelastic analysis led to the choice of beam elements, despite some limitations in capturing detailed stress and deformation profiles compared to shell elements.

2.2 Mass Model

The mass model represents the distribution of mass and inertia properties throughout the aircraft structure. The mass model is crucial because it affects how the aircraft responds to dynamic loads, influences flutter speed predictions, and ensures structural components can handle operational stresses.

Constructing the mass model involves several steps. First, the aircraft is divided into primary components such as wings, fuselage, empennage, engines, landing gear, and payload. Each component's mass is then assigned to corresponding finite element nodes or elements based on their geometry and material properties. Inertia properties, including moments of inertia and products of inertia, are calculated to account for rotational resistance.

Mass is typically represented as lumped masses at discrete points (nodes) within the finite element model. The mass and inertia data are compiled into a global mass matrix that represents the entire aircraft structure. This matrix is used alongside stiffness and aerodynamic matrices in aeroelastic analyses.

For example, in a wing section, the mass is calculated by summing the masses of the skin, ribs, spars, and other components, considering material density and volume. Moments of inertia are computed using standard formulas, considering the mass distribution along the wing's span and chord. These calculated masses and inertia properties are then distributed to the finite element nodes, ensuring accurate representation of each element's mass properties.

2.3 Eigenmodes

The selected structural and mass modeling allows for the calculation of eigenfrequencies and eigenmodes. SOL 103 in *MSC Nastran* is a solution sequence primarily designed for linear static analysis. This method assumes linear material behavior, where stress and strain relationships are considered linear within the elastic range of the material. The key features and considerations of SOL 103 include the assumption of small deformations, meaning that the structural response is within the range of linear elasticity, and it does not account for large displacements or geometric nonlinearity.

The analysis is based on the principle of static equilibrium, assuming that applied loads are balanced by internal resistances within the structure. This makes SOL 103 suitable for scenarios where dynamic effects are negligible compared to static loading conditions. It does not consider the effects of time or dynamic loading, making it a quasi-static analysis.

However, SOL 103 has limitations. It is not suitable for materials exhibiting significant nonlinear behavior, such as plastic deformation or large strain effects. Additionally, the assumption of small deformations restricts its applicability to situations where the structural response remains within the linear range.

The solution sequence SOL 103 was then applied to the aeroelastic model present in Chapter 4. In this solution sequence the mass matrix ($\boldsymbol{M}$) and the stiffness matrix ($\boldsymbol{K}$) are computed. It can be confirm that $\boldsymbol{M}$ and $\boldsymbol{K}$ are real and symmetric, and $\boldsymbol{M}$ is positive semi-definite. Moreover, mass properties such total mass, center of gravity position and inertial properties can be seen and compared to the previsions made.

Real eigenvalues and their associated eigenvectors are extracted, in the case of normal mode analyses, from the equation:

$$[\boldsymbol{K} - w^2 \boldsymbol{M}]\hat{\boldsymbol{v}} = 0 \tag{2.1}$$

being $\hat{\boldsymbol{v}}$ the displacement vector and $\lambda = \sqrt{w^2}$, being λ the eigenvalues. The eigenvalue problem in Equation 2.1, can be very computational demanding to solve, hence a modal approach can be used to reduced the complexity of the problem. In section 2.8.2 modal analyses is explained in a detailed way.

2.4 Aerodynamics Model

In aeroelastic modeling, the aerodynamic model is pivotal for understanding how aerodynamic forces and pressures interact with an aircraft's flexible structure. While for other disciplines only single aerodynamic coefficients of the aircraft are requested , in aeroelasticity the pressure distribution across the surface is important too. This understanding is crucial for predicting the dynamic response, stability, and safety of the aircraft across diverse flight conditions and aerodynamic loads. Implementing the aerodynamic model through the Doublet-Lattice Method (DLM) is the key.

Developed in the late 1960s, the DLM utilizes linearized potential flow to address unsteady aerodynamic loads on lifting surfaces undergoing harmonic motion. It discretizes lifting surfaces, often modeled as thin flat plates, into a lattice of doublets, solving for a flow field adhering to potential flow equations while ensuring flow tangency at the modeled surfaces. Operating in the frequency domain, the DLM is particularly advantageous for aeroelastic stability analyses during incremental motion from equilibrium, facilitating early design phases of aerospace vehicles.

Rooted in earlier methods like Falkner's vortex-lattice method [14], the DLM extends previous work by Hedman [16] from steady to oscillatory flow cases. It approximates lifting surfaces with trapezoidal panels, or "boxes," arranged in columns parallel to the freestream, where each box represents a distribution of acceleration potential doublets (Figure 2.4.1). These doublets' strengths are determined by parameters like force per unit length of the chord line and the length of the line segment.

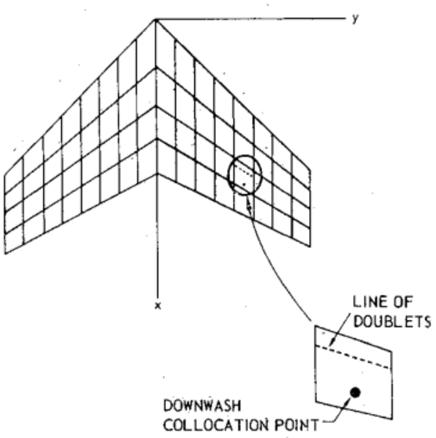

Figure 2.4.1: Surface and panel geometry [1].

A key assumption of the method is that the surface can be represented by line segments of acceleration potential doublets. Though lacking a rigorous analytical basis, numerical experiments confirm its validity for subsonic flows. Additionally, the method assumes uniform chord lengths and strip widths across the surface [1].

Advantages of the DLM include its ability to handle discontinuous normal wash without complex discrimination among surface features and its independence from the properties of the normal wash distribution. This allows a single matrix computed for a wing to yield solutions for various control surface configurations [1].

2.5 Rigid and Elastic Equations of Motion

Evaluating the trim conditions of an aircraft holds paramount importance for multiple reasons, with particular significance in aeroelastic analyses.. They play a crucial role in understanding the interaction between aerodynamic forces and structural deformations. Identifying trim conditions helps anticipate and mitigate aeroelastic effects, such as flutter and divergence, which can arise when dynamic forces and structural deformations interact unfavorably.

Before delving into the intricacies of trim, it is imperative to address the fundamental aircraft equations of motion. Aircraft motion is typically classified into two components: rigid and flexible. In the rigid component, the aircraft is treated as a point mass characterized by inertia matrices $\boldsymbol{M}_b$ and $\boldsymbol{I}_b$. The inertia tensor $\boldsymbol{I}_b$ is specifically computed with respect to the body axis 'b'. All external forces and moments $\boldsymbol{p}_b$ are gathered at the same point. The governing nonlinear equations of motion are expressed as follows:

$$\dot{\boldsymbol{v}}_b = \boldsymbol{M}_b^{-1} \cdot \boldsymbol{p}_b^{ext,forces} + \boldsymbol{v}_b \times \boldsymbol{w}_b + \dot{\boldsymbol{v}}_b^{grav} \tag{2.2}$$

$$\dot{\boldsymbol{w}}_b = \boldsymbol{I}_b^{-1} \cdot (\boldsymbol{p}_b^{ext,moments} - \boldsymbol{w}_b \times (\boldsymbol{I}_b \cdot \boldsymbol{w}_b)) \tag{2.3}$$

being the $\dot{\boldsymbol{v}}_b$ and $\dot{\boldsymbol{w}}_b$ the translational and rotational accelerations, respectively. The coupling terms $\boldsymbol{v}_b \times \boldsymbol{w}_b$ and $\boldsymbol{w}_b \times (\boldsymbol{I}_b \cdot \boldsymbol{w}_b)$ are derived by Waszak, Schmidt, and Buttrill [10, 35, 36].

Concerning the flexible part, the linear structural dynamics are incorporated by

$$\boldsymbol{M}_{ff}\ddot{\boldsymbol{u}}_f + \boldsymbol{D}_{ff}\dot{\boldsymbol{u}}_f + \boldsymbol{K}_{ff}\boldsymbol{u}_f = \boldsymbol{p}_f^{ext} \tag{2.4}$$

being the $\boldsymbol{u}_f$ the linear elastic deflections, $\dot{\boldsymbol{u}}_f$ the velocities, and $\ddot{\boldsymbol{u}}_f$ the accelerations. The matrices $\boldsymbol{M}_{ff}$, $\boldsymbol{D}_{ff}$, and $\boldsymbol{K}_{ff}$ refer to the generalized mass, damping, and stiffness matrices.

At this point, using the aerodynamics forces and the equations of motion, it is important to convert the equations into a first-order system:

$$\begin{pmatrix} \dot{\boldsymbol{u}}_i \\ \ddot{\boldsymbol{u}}_b \\ \dot{\boldsymbol{u}}_f \\ \ddot{\boldsymbol{u}}_f \\ \dot{\boldsymbol{u}}_{cs} \end{pmatrix} = f \begin{pmatrix} \boldsymbol{u}_i \\ \dot{\boldsymbol{u}}_b \\ \boldsymbol{u}_f \\ \dot{\boldsymbol{u}}_f \\ \boldsymbol{u}_{cs} \end{pmatrix} \tag{2.5}$$

$\boldsymbol{u}_i$ encompasses the positional data and Euler angles relative to the earth-fixed frame, while $\dot{\boldsymbol{u}}_b$ represents the velocities and rates within the body-fixed frame. Additionally, $\boldsymbol{u}_{cs}$ contains the control commands.

Finding a solution to Equation 2.5 places the aircraft into an equilibrium state, in other words, the trimmed state. To establish trim conditions effectively, it's crucial to ensure Equation 2.5 remains appropriately constrained. For example, when defining trim conditions for horizontal level flight at a specific airspeed, roll and pitch rates are nullified, allowing freedom in control surface deflections, particularly concerning elevators and ailerons. The solution to Equation 2.5 within the *Loads Kernel* employs Powell's non-linear root-finding algorithm [37]. For deeper insights into this process, please consult [34]. This methodology underwent numerical validation against *MSC Nastran SOL144* [23].

2.6 Maneuver Loads

A flight maneuver is essentially any deviation from straight and level flight initiated by control surface commands like the elevator, rudder, or ailerons. While some maneuvers do not impose significant loads, others are crucial for maintaining structural integrity. Certain maneuvers fall under the category of quasi-steady, where the dominant acceleration terms remain constant over time. For instance, a steady turn with constant radius, airspeed, and altitude exemplifies this. Quasi-steady maneuvers exhibit constant inertial reaction forces and steady aerodynamic forces. These characteristics simplify modeling and computations since the flow relative to the aircraft remains constant.

However, not all maneuvers fit into this quasi-steady framework. Take rapid elevator motion, for example. Analyzing such maneuvers is vital for certifying commercial aircraft. In these cases, a dynamic problem arises due to the quick pull-back of the control stick, causing rapid elevator deflection. The time-dependent buildup of aerodynamic forces introduces a lag effect that must be considered, as the high rate of load change can induce unsteady elastic motion in the aircraft [8]. A way of analysing transient maneuver is to split the maneuver into selected worst-case situation and then analyse them as quasi-steady maneuver load cases.

Inertial reactions refer to the forces and moments experienced by a free-flying aircraft due to external forces and resulting linear and rotational accelerations. These reactions must be considered alongside external forces to achieve dynamic equilibrium, where the resultant sum around the center of mass is zero. In a practical example, such as a transport aircraft in 1-g flight with a full fuel load, inertial forces can reduce structural stress. This relief occurs as inertial loading, including forces like propulsion, aerodynamic, and store separation, redistributes loads, often decreasing the wing-root shear force by a significant margin.

2.7 Gust Loads

In aeronautics, a gust refers to a sudden change in wind speed and/or direction experienced by an aircraft during flight. These atmospheric disturbances can significantly affect the aircraft, causing variations in aerodynamic forces, structural loads, and ride comfort. Gusts can alter lift and drag forces, leading to changes in airspeed, altitude, and attitude, while also imposing additional stress on the aircraft structure, which must be carefully considered during design and certification. Modeling gusts is crucial for understanding and predicting their impact on aircraft performance and safety. Accurate modeling allows engineers to design aircraft structures capable of withstanding gust forces, while pilots can anticipate and respond effectively to maintain control during flight, ensuring the safety of passengers and crew [5].

The earliest studies of aircraft encountering gusts were performed by Pratt [24] and Bisplinghoff [6], with notable contributions from Küssner [26]. Over time, various models have been developed to represent gusts, among which four have been accepted by regulating authorities as acceptable means of compliance for aircraft certification: the Pratt Formula, the Probabilistic Load Factor, the (1-cos) Discrete Gust, and the Continuous Random Turbulence.

The (1-cos) Discrete Gust Model presents several advantages, making it a valuable tool in aeronautical engineering. Its simplicity offers a straightforward representation of gust effects on aircraft, making it accessible for preliminary analyses and conceptual design stages. Moreover, its computational efficiency requires fewer resources compared to more complex models, facilitating quicker simulations and analyses. The model's transparent and interpretable results facilitate better understanding of gust effects. By representing gusts as discrete changes in airspeed using the 1-cosine function, the model provides a focused representation sufficient for many design and certification purposes. Additionally, its versatility allows for easy adaptation to simulate various gust scenarios and study their effects on different aircraft configurations. Overall, the (1-cos) Discrete Gust Model strikes a balance between simplicity and effectiveness, making it a valuable tool for initial design assessments and rapid analyses in aeronautical engineering. Hence, it warrants particular attention in research and application.

In the (1-cos) Discrete Gust model, the gust shape is defined as follows:

$$U = \frac{U_{ds}}{2}(1 - \cos(\frac{2\pi s}{2H})) \tag{2.6}$$

Here, U_{ds} represents the design gust velocity, s denotes the distance penetrated into the gust, and H stands for the gust gradient, which signifies the distance parallel to the airplane's flight path for the gust to reach its peak. The basic shape of the 1-cos gust is illustrated in Figure 2.7.1.

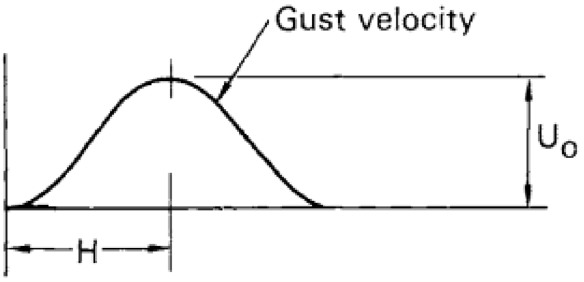

Figure 2.7.1: Shape and velocity of the basic 1-cos gust [19].

According to certification specifications for large airplanes outlined in CS-25.341 [11], a range of gust gradient distances from 9 m (30 feet) to 107 m (350 feet) must be explored to determine the critical response for each load quantity.

The design gust velocity is calculated as:

$$U_{ds} = U_{ref} F_g (\frac{H}{107})^{\frac{1}{6}} \tag{2.7}$$

Here, U_{ref} denotes the reference gust velocity in equivalent airspeed, and F_g represents the flight profile alleviation factor.

Regarding the reference gust velocities, CS-25.341 [11] specifies that between speeds V_B and V_C, U_{ref} equals 17.07 m/s EAS at sea level. The reference gust velocity linearly decreases from 17.07 m/s EAS at sea level to 13.41 m/s EAS at 4572 m, and further decreases to 6.36 m/s EAS at 18288 m. At the aircraft diving speed V_D, U_{ref} is set to 0.5 times the value obtained for speeds between V_B and V_C.

The reference gust velocity, assumed with a gradient distance of 107 meters, represents a single peak event occurring every 70000 hours if the plane were to fly 100 percent of its service life at the respective altitude. Initially, it is normalized by the gust gradient to account for the reduced reference velocity of gust with shorter gradients. Subsequently, an alleviation factor F_g is applied to accommodate the specific mission profiles of the considered aircraft, based on the anticipated service time at each altitude. The profile alleviation factor F_g increases linearly from the sea level value to a level of 1.0 at the maximum operating altitude.

2.8 Flutter

Flutter represents the self-sustained oscillation of an aircraft's structure caused by unsteady aerodynamic forces. Over time, these oscillations can intensify, posing a serious risk of structural failure. To address the flutter phenomenon, understanding unsteady aerodynamics is imperative. One approach to investigate flutter stability involves time-domain simulations. Starting from Equation 2.4, neglecting the damping matrix and considering as external forces only the aerodynamic forces, the motion is described by solving:

$$\boldsymbol{M}\ddot{\boldsymbol{v}} + \boldsymbol{K}\dot{\boldsymbol{v}} = \boldsymbol{f}_a(t) \tag{2.8}$$

$\boldsymbol{M}$ represents the mass matrix, $\boldsymbol{K}$ denotes the stiffness matrix, $\boldsymbol{f}_a(t)$ embodies aerodynamic forces, and $\dot{v}$ signifies the displacement vector.

However, analyzing the stability of linear systems is more conveniently achieved in the frequency domain. By focusing on external forces dependent of elastic deformation, the frequency-domain equations of motion can be formulated as:

$$\boldsymbol{M}p^2\hat{\boldsymbol{v}} + \boldsymbol{K}\hat{\boldsymbol{v}} = q\boldsymbol{Q}(\hat{p})\hat{\boldsymbol{v}} \tag{2.9}$$

Here, the aerodynamic transfer matrix $\boldsymbol{Q}(\hat{p})$ relies on the reduced Laplace variable $\hat{p} = \frac{p\bar{c}}{2u}$, with $\bar{c}$ representing the mean wing chord. Rearranging the frequency-domain equations (2.9), the nonlinear eigenvalue problem is derived:

$$\boldsymbol{F}(p)\hat{\boldsymbol{v}} = [\boldsymbol{M}p^2 + \boldsymbol{K} - q\boldsymbol{Q}(\hat{p})]\hat{\boldsymbol{v}} = 0 \tag{2.10}$$

p serves as the eigenvalue rendering the flutter matrix $\boldsymbol{F}(p)$ singular, while $\hat{\boldsymbol{v}}$ denotes the eigenvector. This problem is nonlinear because $\boldsymbol{F}(p)$ exhibits dependence on p in a nonlinear manner.

The stability of an aeroelastic mode is discerned by the real part of the eigenvalue. If all eigenvalues possess negative real parts (Re p_j < 0), the structure maintains aeroelastic stability. However, if an eigenvalue crosses the imaginary axis (i.e., the real part of one eigenvalue becomes positive), the mode undergoes flutter instability, leading to undamped vibrations in the structure. The velocity at which this phenomenon occurs is termed the flutter velocity $V_{flutter}$ [8].

2.8.1 P-K Method

Many aerodynamic methods, such as the doublet-lattice method [1], employed in aeroelastic stability analyses, provide frequency-domain forces $\boldsymbol{Q}(k)$, where $k = \mathrm{Im}p$, rather than a transfer matrix $\boldsymbol{Q}(\hat{p})$. At the flutter boundary, the structure exhibits undamped vibrations, indicating that the forces $\boldsymbol{Q}(k)$ accurately represent conditions at this critical point and offer a reasonable approximation for weakly damped motion. Consequently, a flutter solution $\hat{p} = ik$ to the approximate eigenvalue problem

$$\left[\left(\frac{u}{b}\right)^2 \boldsymbol{M}p^2 + \boldsymbol{K} - q\boldsymbol{Q}(k)\right]\hat{\boldsymbol{v}} = 0 \tag{2.11}$$

will also satisfy the full nonlinear eigenvalue problem 2.10. Essentially, both eigenvalue problems yield the same flutter speed, although 2.11 provides only approximate eigenvalues $\hat{p}$ for subcritical speeds.

Assuming that the aerodynamic matrix $\boldsymbol{Q}(k)$ is given, the task is now to solve the eigenvalue problem 2.11 for a given airspeed. The essence of the p-k method lies in iteratively solving this problem, treating k in $\boldsymbol{Q}(k)$ as a parameter. For a specified k value, a linear eigenvalue problem can be tackled to obtain a set of eigenvalues $\hat{p}_j^2(k)$, from which the positive-frequency square roots $\hat{p}_j(k)$ are considered. Should any of these solutions $\hat{p}_j(k)$ satisfy Im$\hat{p}_j(k) = k$, it must correspond to an eigenvalue $\hat{p}$ in 2.11. Details on finding solutions to the nonlinear scalar equation 2.11 are elaborated in Bäck and Ringertz [4].

At a given airspeed u, employing the p-k algorithm enables computation of a set of eigenvalues $\hat{p}_j$ and corresponding eigenvectors $\hat{v}_j$ for the nonlinear eigenvalue problem 2.11. Typically, only a subset of potential eigenvalues is computed, as the flutter mechanism primarily involves low-frequency modes [8].

2.8.2 Modal Analyses

The eigenvalue problem 2.11 poses significant computational demands, particularly for aircraft structures with thousands of degrees of freedom. To enhance efficiency, a reduced set of modal coordinates can be introduced. Initially, the vibration eigenvalue problem must be addressed:

$$[\boldsymbol{K} - w^2\boldsymbol{M}]z = 0 \tag{2.12}$$

yielding a set of n eigenvalues w_j^2 and corresponding modeshapes z_j. Despite the inclusion of aerodynamic forces, aeroelastic motion remains largely influenced by low-frequency structural modes. Hence, the aeroelastic motion can be approximated as:

$$\hat{\boldsymbol{v}} = \eta_1 z_1 + \eta_2 z_2 + \ldots + \eta_m z_m = \boldsymbol{Z\eta} \tag{2.13}$$

η_j denotes a new set of m modal coordinates, and the columns z_j of the $n \times m$ matrix $\boldsymbol{Z}$ delineate the subspace where the aeroelastic motion is restricited.

By normalizing the eigenvectors z_j such that the $m \times m$ generalized mass and stiffness matrices satisfy $\boldsymbol{Z}^T\boldsymbol{MZ} = \boldsymbol{I}$ and $\boldsymbol{Z}^T\boldsymbol{KZ} = \boldsymbol{\Omega} =$ diag(w_j^2) respectively, the equations of motion in terms of modal coordinates take on nondimensional form, constituting the flutter eigenvalue problem:

$$[\boldsymbol{I}\hat{p}^2 + (\frac{b}{u})^2\boldsymbol{\Omega} - \frac{\rho b^2}{2}\hat{\boldsymbol{A}}(k)]\boldsymbol{\eta} = 0 \tag{2.14}$$

where $\hat{\boldsymbol{A}}(k) = \boldsymbol{Z}^T\boldsymbol{Q}(k)\boldsymbol{Z}$ represents the $m \times m$ generalized aerodynamic matrix. Initially solved for a set of eigenvalues w_j^2 and eigenvectors z_j, the size of the flutter eigenvalue problem can then be adjusted. It is crucial to note that an excessively small basis $\boldsymbol{Z}$ may inadequately represent true motion, resulting in inaccurate flutter results. Typically, the problem is solved using a small basis, progressively expanded until convergence of flutter results is achieved.

The flutter frequency w_F and modeshape $\boldsymbol{\eta}_F$ are determined using the p-k method, while the original flutter modeshape $\hat{v}_F$ can be reconstructed from 2.13. The modal flutter modeshape contains information regarding the contribution of different structural modes to flutter motion, encompassing both magnitude and phase shift. Consequently, the magnitude of elements in $\boldsymbol{\eta}_F$ is often denoted as modal participation coefficients [8].

Chapter 3

Aircraft Selection

To ensure the generality, requisite complexity, and representativeness of the developed aeroelastic model, a deliberate choice was made regarding the optimal aircraft. To comprehend the rationale behind this selection, it is imperative to first grasp the specific requirements that the chosen aircraft needed to fulfill. The decision was made to start with an existing aircraft and, if needed, introduce modifications to accentuate certain aeroelastic phenomena.

3.1 Aircraft Requirements

The outlined requirements were carefully devised to strike a balance between achieving a suitable level of complexity/simplicity, thoroughly testing the software's features, and capturing aeroelastic phenomena. The aim was to select a generic and representative aircraft. The specific requirements and specifications targeted are as follows:

- **Aircraft Configuration:** Simple and conventional.
- **Wing:** Features a simple planform (non-rectangular), with a significant leading edge (LE) sweep angle (Λ_{LE}), washin/washout angle (Φ), dihedral angle (Γ), and an airfoil with camber. The aspect ratio ($\boldsymbol{AR}$) should exceed 8 to facilitate the application of beam theory.
- **Empennage:** Adheres to a conventional configuration or includes a T-tail.
- **Control Surfaces:** Includes ailerons, elevators, and a rudder. Flaps, though

optional, are excluded from the model.

- **Engines:** Limited to a maximum of 2 engines.
- **Subsonic Regime:** Mach number is below 0.6 ($Ma < 0.6$) to avoid the formation of shock waves.
- **Representativeness:** The aircraft must be easily recognizable, as well as representative; for instance, a glider is not deemed suitable.
- **Information Availability:** Extensive data about the aircraft must be publicly accessible. This encompasses general geometry dimensions, airfoil data, internal structure, center of gravity (Cg), mass distribution, flight envelope, and performance.
- **Aeroelastic Effects:** The aircraft should exhibit notable wing bending and torsion during level flight, with an evident flutter mechanism where bending and torsion modes are coupled. It is noteworthy that the properties of the aircraft can be manipulated to accentuate these aeroelastic phenomena.

3.2 Aircraft Comparison

After carefully reviewing the specifications outlined in Section 3.1, an exhaustive search was conducted to identify an aircraft that meets all the specified criteria. A notable challenge encountered during this search was the prevalence of subsonic aircraft with either no sweep angle or very low sweep angles in their wings. This is attributed to the use of straight wings in subsonic aircraft to enhance lift efficiency and ensure predictable stall behavior at lower speeds, thereby complicating the task of finding an aircraft that satisfies both requirements.

The aircraft comparison in Table 3.2.1 showcases various selected options, each either meeting or closely approaching the specified criteria for aircraft selection.

Examining Table 3.2.1 reveals that all four aircraft operate within the subsonic regime and are equipped with two wing-mounted engines. With the exception of the Douglas DC-3, which adopts a conventional configuration, the remaining aircraft feature a T-tail configuration. Notably, the Aspect Ratio surpasses the required minimum of eight for each of the four aircraft. The Douglas DC-3 stands out with a significant leading edge sweep, while both the Dornier 328 and ATR 42 exhibit no

	Dornier 328	**ATR 42**	**Embraer 120**	**Douglas DC-3**
Aircraft Type	commercial	commercial	commercial	commercial/military
Flight Regime	subsonic	subsonic	subsonic	subsonic
Tail Configuration	T-tail	T-tail	T-tail	conventional
N° of Engines	2	2	2	2
Aspect Ratio	11.0	11.1	9.9	9.2
Wing LE Sweep	<5°	<5°	<5°	15.5°
Wing Dihedral	0°	0°	7.5°	5°

Table 3.2.1: Aircraft characteristics comparison.

wing dihedral, a design choice influenced by their wings being mounted on top of the fuselage.

Given that the Douglas DC-3 aligns more decisively with all specified requirements, especially in terms of the wing leading edge sweep, it emerged as the chosen aircraft. Additionally, the DC-3 holds greater representativeness, having served in both commercial and military capacities since 1936 [38]. Its historical significance and widespread recognition further supported this selection. Another contributing factor was the wealth of open-source information available for the DC-3, facilitating a more comprehensive analysis.

3.3 Douglas DC-3

The Douglas DC-3 (Figure 3.3.1), a propeller-driven airliner crafted by the Douglas Aircraft Company, left an permanent mark on aviation from the 1930s to 1940s and during World War II. Evolving from the DC-2, it emerged as a larger, improved 14-bed sleeper with a low-wing metal monoplane design, conventional landing gear, and two radial piston engines. Initially featuring the Wright R-1820 Cyclone for civil service, later versions adopted the Pratt & Whitney R-1830 Twin Wasp engine. With a cruising speed of 333 km/h, a capacity for 21 to 32 passengers or 2,700 kg of cargo, and a range of 2,400 km, the DC-3 showcased exceptional performance, allowing operation from short runways.

Setting new standards in air travel, the DC-3 excelled in speed, reliability, and passenger comfort. Pioneering transcontinental routes, it completed New York to Los Angeles journeys in 18 hours with only three stops. A groundbreaking airliner, it achieved profitability solely from passenger services, eliminating the need for mail subsidies.

Post-World War II, market saturation with surplus aircraft challenged the DC-3's competitiveness against faster models. Despite this, its adaptability found utility in less commercially demanding routes. Civilian production ceased in 1943 at 607 aircraft. Military variants, including the C-47 Skytrain, and global productions totaled over 16,000. Approximately 150 DC-3s remain operational as of 2023, underscoring its enduring legacy [38].

Figure 3.3.1: A DC-3 operated in period Scandinavian Airlines colours by *Flygande Veteraner* flying over Lidingö, Sweden, in 1989 [38].

Subsequently, the general characteristics and performance capabilities of the DC-3 are presented, with a specific focus on the DC-3A variant, as detailed in [3, 25]. Figure 3.3.2 provides visual representations of the aircraft's three views.

General characteristics:

- **Length (l):** 19.7 m
- **Wingspan (b):** 29.0 m
- **Height (h):** 5.16 m
- **Wing area (S):** 91.7 m^2
- **Airfoil:** NACA 2215 (wing root), NACA 2206 (wing tip)
- **Empty weight ($\mathbf{W}_e$):** 7649 kg

- **Maximum take-off mass ($MTOM$):** 11 884.12 kg
- **Powerplant:** 2 × Pratt & Whitney R-1830-S1C3G Twin Wasp 14-cyl. air-cooled two row radial piston engine, 890 kW each
- **Propellers:** 3-bladed Hamilton Standard 23E50 series, 3.5 m diameter hydraulically controlled constant speed, feathering

Performance:

- **Cruise Speed (V_C):** 339 km/h
- **Never exceed speed (V_{NE}):** 413 km/h
- **Stall Speed (V_S):** 125.9 km/h
- **Range (R):** 2 540 km
- **Service ceiling:** 7,100 m
- **Rate of climb (ROC):** 5.8 m/s
- **Wing loading (W/S):** 125 kg/m^2
- **Power/mass (P/M):** 156.5 W/kg

The Douglas DC-3 is an all-metal, low-wing monoplane with retractable landing gear featuring a tail wheel. Powered by Pratt and Whitney R1830-3103G engines, it accommodates a maximum crew of four: a Captain, a First Officer, a Cabin Attendant, and an Observer.

The fuselage employs semi-monocoque construction with transverse frames and longitudinal members covered by 24ST Alclad sheet. The wing is a full cantilever, multi-cellular stressed-skin structure, divided into a center section and two outer panels. The outer panels have three metal spars, hydraulically operated split trailing edge flaps, and fabric-covered, statically and aerodynamically balanced ailerons.

The empennage features a large vertical stabilizer and rudder, constructed with full cantilever, metal skin multi-cellular design. Elevators and rudder are fabric-covered, metal frame construction with ball bearing hinges and controllable trimming tabs.

The landing gear consists of two independent units retracting into the nacelles,

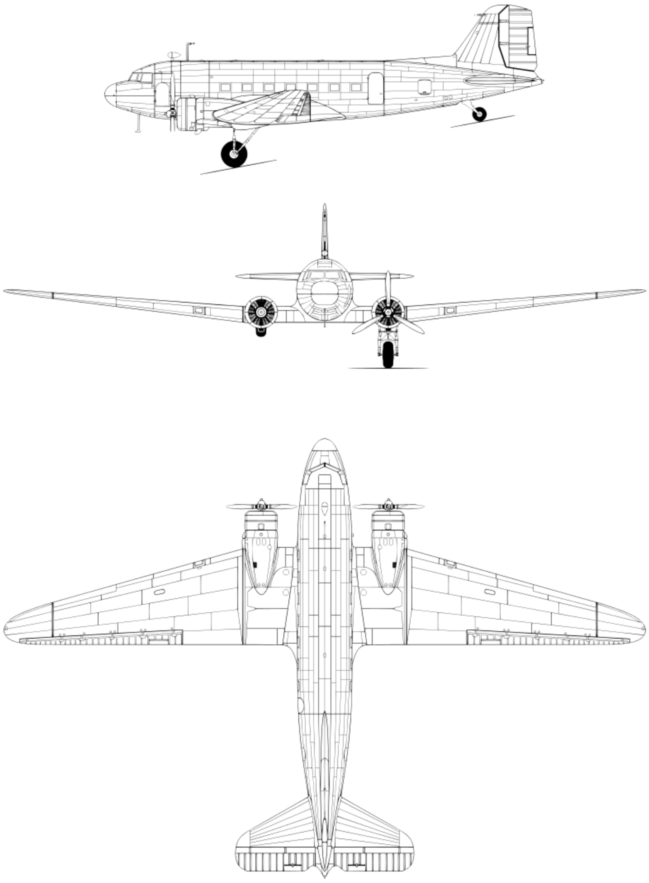

Figure 3.3.2: Three-view drawing of the Douglas DC-3 [38].

mounted on oleo type shock absorber struts. The hydraulic retracting mechanism takes less than 30 seconds to fully retract or extend, with safety latches for landing position. Flight wheel brakes prevent wheel rotation after retraction, eliminating the need for pilot intervention during the process.

Chapter 4

Aeroelastic Model

After selecting the aircraft in Chapter Three as the starting point, the development of the aeroelastic model will commence. This model will include the finite element model, aerodynamic model, mass model, and fuel model. In this chapter, each of these components will be presented and explained. Additionally, the different mass configurations and various modified models will be detailed. Finally, the eigenmodes of the final modified model will be analyzed.

4.1 Finite Element Model

To construct the finite element model for the Douglas DC-3, *ModGen* was employed, an in-house tool developed by DLR. *ModGen*, a *Fortran77* program, specializes in generating finite element models within *MSC Nastran*, specifically tailored for aircraft components such as wing-like and fuselage structures. Additionally, *ModGen* facilitates the creation of input cards for structural optimization and aeroelastic analysis, enhancing its versatility and utility in the aircraft modeling process [20].

4.1.1 Planform Definition

ModGen was utilized in the DC-3 case to establish the Finite Element Model (Finite Element Model (FEM)) for the right and left wings, right and left horizontal tails, and the vertical tail—essentially, all wing-like components. The initial step involved defining the planform of these components. This was achieved by referencing the technical drawing available in [3] (Figure 4.1.1) and the general specifications of the airplane outlined in the same report.

Geometrical parameters without specific information were extrapolated from the technical drawing using the appropriate scale relative to the actual aircraft. Although there is inherent uncertainty in these measurements, for the purposes of the model as an illustrative example of a generic aeroelastic simulation, the precision of these measures is not critical. For instance, insufficient information about control surfaces dimensions led to an approximation of their geometry, ensuring that the areas matched those specified in the report. Furthermore, for questions of simplicity flaps were not modelled.

Certain approximations were made, particularly concerning the tips of the lifting surfaces. As depicted in Figure 4.1.1, the tips of the wing and tail surfaces are rounded. To simplify the geometry and mitigate issues associated with very small edges, the tips were modeled as straight lines instead of rounded.

It is pertinent to note some parameters not explicitly detailed in the technical drawing in Figure 4.1.1 but are nonetheless significant. For the wing, the outer section features a dihedral angle (Γ) of 5° , and the entire wing has an incidence angle (α_i) of 2°. The horizontal tail exhibits a 0° dihedral angle (Γ) and an incidence angle (α_i) of 0°. This detailed information about the aircraft geometry can be consulted in [3], Table I.

Another consideration pertains to the reference point for these dimensions. The chosen reference point is 2 meters in front of the aircraft nose and at the same height as the wing root leading edge. This selection ensures that all dimensions have positive values. The 2-meter margin was incorporated to allow for potential geometry modifications, maintaining positive dimensions without necessitating a shift in the reference point's position.

4.1.2 Airfoils

Once the planform is established, the next step involves assigning airfoils to different surface sections. For the wing, the inner rectangular section adopts the NACA 2215 airfoil. The outer section undergoes an airfoil transition from NACA 2215 at the wing kink to NACA 2209 at the wing tip.

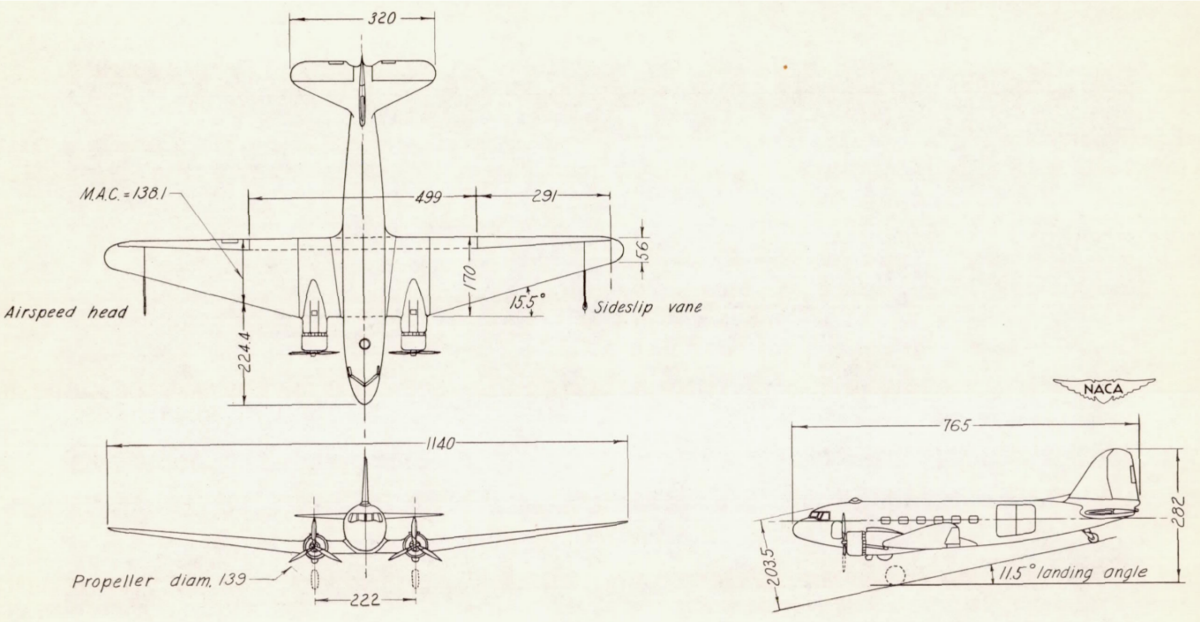

Figure 4.1.1: Three-view drawing of a Douglas DC-3. All dimensions in inches [3].

In the case of the horizontal and vertical tails, specific information about the airfoil used was unavailable. Assuming symmetry, which is typical for this aircraft type, and considering a four-digit NACA series airfoil, it was deduced from the technical drawing that the thickness-to-chord ratio (t/c) for both the horizontal and vertical tails was approximately 10%. Consequently, the NACA 0010 airfoil was employed to model both surfaces.

4.1.3 Spars and Ribs

Shifting the focus to spar modeling, it is crucial to determine the number and precise positions of the spars. Regarding the location of wing spars, detailed information can be found in [25], specifying their positions relative to the wing chord. The wing comprises three spars: a front spar, a center spar, and a rear spar, positioned at 17.65%, 38.80%, and 60.00% of the wing chord, respectively.

To streamline the modeling process, it was decided to model only two of the three spars—specifically, the front and rear spars. However, to account for the contribution of the third spar, the stiffness and mass properties of the modeled spars encompass its effects. Consequently, the Load Reference Axis (LRA) is defined as the center line between the front and rear spars, effectively positioned at the center of the wingbox. The LRA is an imaginary line used as a reference for aerodynamic forces acting on an aircraft's wing.

It is important to note an approximation made during this process. In sections of the wing where ailerons are present, the load reference axis is typically shifted slightly forward because the aileron does not significantly contribute to the stiffness of that section. However, for the sake of simplicity, this forward shift in the LRA was not implemented.

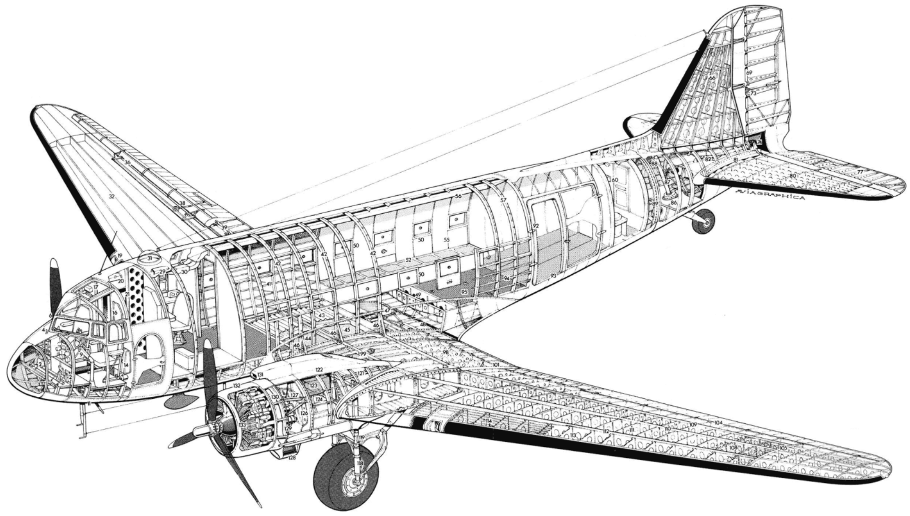

Figure 4.1.2: Douglas DC-3 cutaway drawing [9].

Information on the number and placement of horizontal and vertical tail components was not found in [3, 25]. The Douglas DC-3 cutaway drawing in Figure 4.1.2 was utilized instead. The drawing indicates that both the horizontal and vertical tails have 5 spars each. Although specific positions were not detailed, it was assumed, based on the drawing and industry norms, that the spars were evenly spaced along the chord without control surfaces. Important to refer that, as in the wing case, only the front and rear spars were modelled, and the LRF was positioned in the center of the wing box.

Regarding ribs, limited information was available for both wing and tail in [3, 25]. Again, the cutaway drawing in Figure 4.1.2 guided the analysis. Each wing comprises a total of 31 ribs, with 8 in the inner section (including root and kink ribs) and the remaining evenly distributed in the outer section. Inner section rib placement was manually adjusted to align the sixth rib with the end of the fuel tank, which starts at the wing root.

Similarly, for the horizontal and vertical tails, the drawing was referenced. It was determined that each horizontal tail has 8 equally spaced ribs along the half span, while the vertical tail has 9 equally spaced ribs.

The stringers were not explicitly modeled, but their impact on stiffness properties was incorporated afterward. In Figure 4.1.3 it is possible to see the resulting geometry of the DC-3 model.

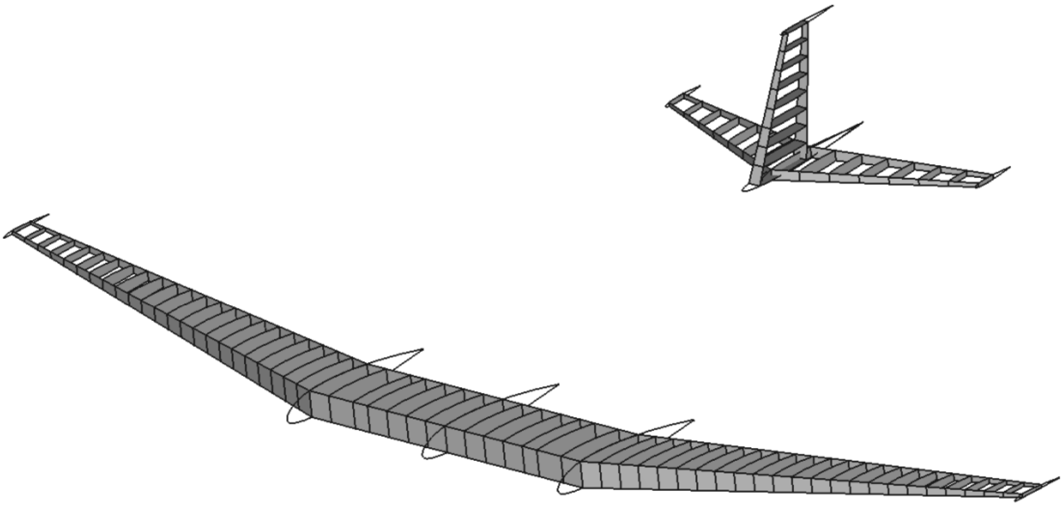

Figure 4.1.3: Douglas DC-3 model geometry.

4.1.4 Materials

In the modeling process, it is crucial to assign a material to the geometry. In this instance, certain assumptions were made to streamline the modeling process. Instead of employing different materials for the wing skin, spars, and ribs, a single material was utilized. The only known information about the material was that was an aluminium alloy. Because all aluminium alloy have similar material properties (Young's Modulus ($\boldsymbol{E}$) and a Shear Modulus ($\boldsymbol{G}$)), this assumption made is quiet acceptable. Aluminum, known for its favorable strength-to-weight ratio and corrosion resistance, was a common selection for aircraft construction.

The same material was applied to all elements constituting the horizontal and vertical tail. Another justification for this assumption is that material property values might require tuning to ensure the aircraft exhibits an easily observable flutter mechanism.

After consulting tabulated values for the chosen aluminum alloy, a mass density (ρ) of 2710 kg/m^3 was selected. Young's Modulus ($\boldsymbol{E}$) was set at 70 GPa, and the Poisson Ratio (γ) at 0.3. Utilizing the relationship $E = 2(1+\gamma)G$, a Shear Modulus ($\boldsymbol{G}$) of 26.9 GPa was computed.

4.1.5 Structure Model

In the subsequent phase of constructing the Douglas DC-3 model, the definition of stiffness properties took precedence. It is relevant to refer that the aircraft model was initially done to be as close as possible to the reality. Nevertheless, it is intended to develop more flexible versions of the model so that the objectives of the model are fulfilled. Because it is intended to modify the stiffness properties, these ones were determined in a manual process using *Python* scripts.

The wing-like components, comprising the wing, Horizontal Tail (HT), and Vertical Tail (VT), were modeled as beams along their Load Reference Axis (LRA). For example, consider the right wing with 31 ribs, resulting in 31 grid points along the LRA. Stiffness properties were prescribed in the regions between these grid points leading to 30 section, each of them requiring the definition of properties such as cross-sectional area ($\boldsymbol{A}$), area moment of inertia about the chordwise axis ($\boldsymbol{I}1$), area moment of inertia about the axis perpendicular to the chordwise direction in the airfoil plane ($\boldsymbol{I}2$), and torsional constant ($\boldsymbol{J}$). In Figure 4.1.5 it is possible to see the LRA, as well as the LRA grid points and the associated Leading Edge (LE) and Trailing Edge (TE) grid points.

Figure 4.1.4: Douglas DC-3 wing being assembled [32].

The computation of these cross-sectional properties involved considering the contributions of spars, skin, and stringers (in the case of the wing). Spar cross-sections were approximated as rectangular, with their height derived from airfoil coordinates and spar positions. Spar thickness was more challenging and was extracted from images of the aircraft being assembled, as illustrated in Figure 4.1.4, through reverse engineering techniques. For skin contributions, the airfoil shape was approximated to an elliptical form, making the skin a hollow ellipse. In the case of the wing, the skin thickness ($\boldsymbol{t_{ws}}$) accounted for both the actual skin thickness and the contribution from the stringers, formulated as $t_{ws} = t_{ws} + \frac{2}{5}t_{str}$, where t_{str} represents the stringers' thickness extracted from Figure 4.1.4, and the $2/5$ factor acknowledges that stringers cover only about $2/5$ of the airfoil surface.

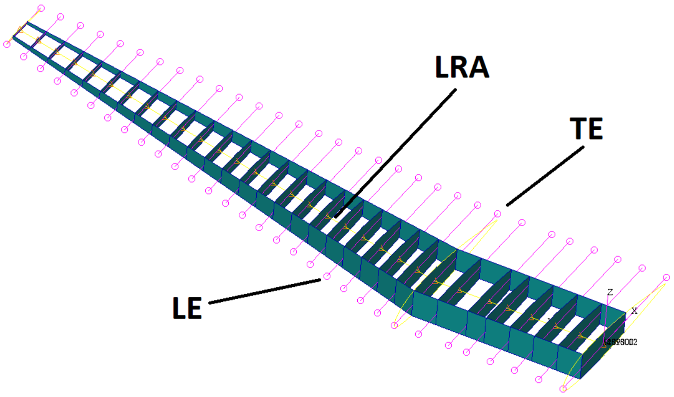

Figure 4.1.5: Douglas DC-3 right wing model with the nodes, LRA, spars and ribs.

All dimensions used in the property calculations were parametrically dependent on the chord, allowing for straightforward and logical generation of properties along the surfaces' span. Figure 4.1.6 displays the area moments of inertia along the span of the right wing. It is seen that these properties magnitude decreases towards the wing tip as expected.

For the tail surfaces, a similar methodology was applied. Although there were no available images of the empennage assembly, the assumption was made that spar and skin thicknesses followed the same relation with the chord as in the wing case. This assumption proved reasonable, as subsequent mass calculations and comparisons allowed for fine-tuning of these thicknesses.

	Wing	**HT**	**VT**
t_{skin} $[mm]$	3.40	2.10	3.46
t_{spar} $[mm]$	4.62	3.00	4.42
t_{str} $[mm]$	0.41	-	-

Table 4.1.1: Final thickness dimensions of the different spars, skins and stringers.

To ensure the accuracy of the dimensions estimated for the spars, skins, and stringers, comprehensive mass calculations were conducted. By incorporating data on cross-sectional areas, lengths of distinct sections, and material density, it became feasible to determine the total mass of the wing, horizontal and vertical tail. This allowed for a thorough comparison with the component mass estimations outlined in Subsection 4.2.1. To achieve alignment with these dimensions, adjustments were made to the thicknesses of spars, skin, and stringers. The final values are presented in Table 4.1.1. It's worth noting that the height estimation of the wing, horizontal and vertical tail spars was very precise. This precision stemmed from extracting the information directly from the airfoil geometry, leveraging the exact knowledge of their positions. It is noteworthy that area moment of inertia and torsional constants were computed relative to the LRA, utilizing the Parallel Axis Theorem.

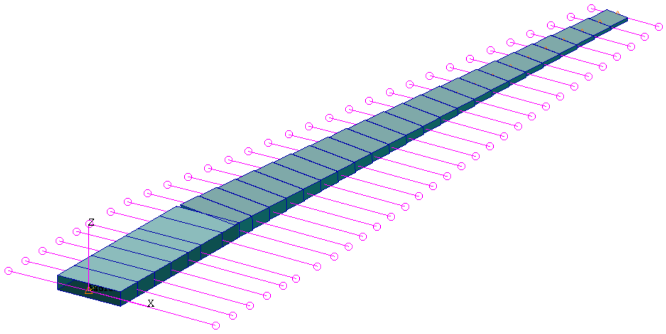

Figure 4.1.6: Douglas DC-3 right wing model displaying the area moments of inertia along the span.

On the contrary, the fuselage and the attached engines were conceptualized as a single rigid body featuring independent degrees of freedom specified at a central grid point, alongside dependent degrees of freedom pinpointed at various grid points. The fuselage was discretized into 11 grid points: one at the aircraft's nose, one at the rearmost part, and the remaining evenly spaced between these two. These fuselage grid points align with the symmetry plane of the aircraft, situated at 1.55 meters above the reference point. This altitude was selected to position the grid points approximately at the center of mass for each cross-section.

Each engine was discretized into 3 grid points, all rigidly connected to the sixth grid point of the corresponding wing. Additionally, the wings and fuselage were interconnected with rigid connections, linking the wing root grid point to the fourth fuselage grid point. The horizontal and vertical tail were also rigidly connected to the fuselage at the tenth grid point.

The decision to model the fuselage as a rigid body, rather than a flexible beam, aimed to maintain model simplicity. This simplification facilitates the identification of specific wing modes when analyzing eigenmodes.

Other aircraft components, not integral to the structure such as systems and payload masses, were not incorporated into the structural model. However, in the mass model, these components are treated as lumped masses, acknowledging their mass without delving into structural intricacies. In Figure 4.1.7 the structural discretization of the model can be seen.

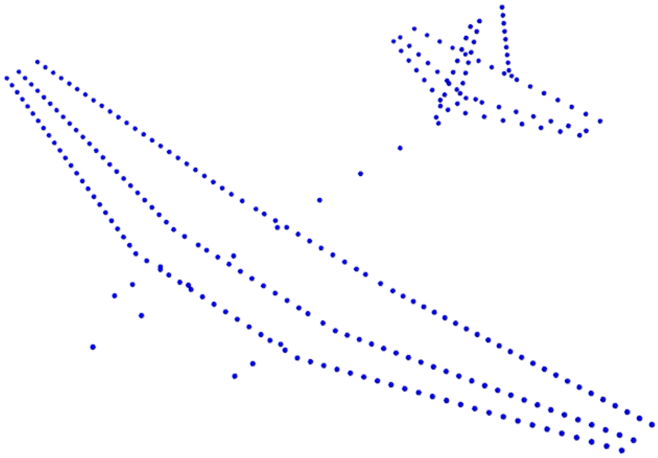

Figure 4.1.7: Douglas DC-3 structural discretization for aeroelastic analyses.

4.2 Mass Model

In this chapter the developed of the mass model is discussed. The first step was to obtain an estimation for the masses of the different aircraft components. Afterwards, the distribution of the estimated masses throughout the aircraft is explained. And, to finalize the chapter, the fuel modeling is discussed in particular, because of its extra complexity.

4.2.1 Mass Estimation of Aircraft Components

Statistical weight estimation methods rely on historical data gleaned from existing airplanes. For instance, by knowing the wing structure weight of a group of aircraft within a specific class, it becomes possible to formulate relationships based on geometric parameters such as wing area, aspect ratio, taper ratio, ultimate load factors, and more. The underlying assumption is that the wing weights of two different aircraft in the same class, certified to the same regulations and with similar gross weights, should exhibit similarity, even when produced by different manufacturers. The statistical relationships established for the entire class of aircraft can, therefore, be leveraged to estimate the wing weight of any aircraft within that class falling between the extremes of the class. These methods typically necessitate the establishment of certain dimensions beforehand. It's worth noting that such methods are often developed primarily for aluminum aircraft, and the increasing use of composites may introduce biases in the resulting weights [15].

The Douglas DC-3, being an aircraft developed and manufactured in the 1930s, adheres to materials and manufacturing techniques consistent with those anticipated by these statistical methods. The equations utilized for weight predictions are tailored for conventional general aviation aircraft, presuming an aluminum aircraft structure. However, adjustments are required when dealing with composite aircraft. The methodologies employed draw from the works of Raymer [27], Torenbeek [33], and Anderson [2] from the Air Force Flight Dynamics Laboratory (USAF).

It is essential to recognize that these equations are valid only under specific conditions, necessitating careful evaluation before implementation. Engineering judgment was applied to discern and exclude specific equations. The selected methods align with the same class as the Douglas DC-3. The components considered include the wing, horizontal and vertical tail, fuselage, landing gear, installed engine, fuel system, flight control system, hydraulic system, avionics, electrical system, air conditioning, and furnishings. The final mass estimation for each component was determined by averaging the valid prediction methods for the DC-3. Instances where a method's estimation seemed illogical led to its exclusion.

To validate the results, the mass estimations for all components were summed and compared against the empty weight ($\boldsymbol{W_E}$) of the aircraft. In cases where a perfect match was not achieved, a scaling factor was applied. For the DC-3, the weight mass estimations were 5.7% lighter than the actual empty aircraft weight, necessitating a scaling factor of 1.06. The scaling factor obtained is very close to 1, revealing that the mass predictions were surprisingly good giving confidence in the reasonableness of the estimations.

Table 4.2.1 presents the weight mass estimations for various aircraft components, along with the empty mass after the application of the scaling factor.

Components	**Mass** $[kg]$
Wing	1616.3
Horizontal Tail	151.2
Vertical Tail	115.2
Fuselage	1407.8
Installed Engine	1883.8
Landing Gear	310.7
Fuel System	207.1
Flight Control System	241.9
Hydraulic System	12.5
Avionics	142.3
Electrical System	255.9
Air Conditioning	608.0
Furnishings	696.3
Empty aircraft weight	7649.0

Table 4.2.1: Weight mass estimations for the different components.

It is crucial to delineate the specific inclusions for each aircraft component. The weight of the wing encompasses not only the wing structure but also incorporates ailerons, flaps, and wingtip fairings. Notably, fuel tanks are excluded from this category. The horizontal tail weight comprises the stabilizer and elevator, while the vertical tail weight includes the fin and rudder. For the fuselage weight, it encompasses the fuselage shell and the associated internal structure but does not incorporate furnishings. For detailed information about what the different aircraft components include, please consult [15].

4.2.2 Components Mass Model

After obtaining mass estimations for various aircraft components, it becomes imperative to strategize their distribution throughout the aircraft.

Starting with the wing-like component, the methodology applied was consistent across the wing, horizontal tail, and vertical tail. To illustrate, with the total weight of the component determined, the next step involves distributing this weight among the component nodes. The decision was made to allocate the total mass as smaller masses situated at the LRA nodes, assuming the center of mass of each cross section to be located in the LRA. The distribution process takes into account the cross-sectional area of different sections.

The allocation was executed for the right and left wing, as well as the right and left horizontal tail, along with the vertical tail. This involved performing a weighted average. The equations for the right and left wing case are presented in Equation 4.1, the right and left horizontal tail case in Equation 4.2, and the vertical case in Equation 4.3.

$$m_i = \frac{m_{wing}}{2} \cdot \frac{A_i}{\sum_{j=1}^{n} A_j} \tag{4.1}$$

$$m_i = \frac{m_{ht}}{2} \cdot \frac{A_i}{\sum_{j=1}^{n} A_j} \tag{4.2}$$

$$m_i = m_{vt} \cdot \frac{A_i}{\sum_{j=1}^{n} A_j} \tag{4.3}$$

The mass in each node, denoted as m_i, is determined based on the cross-sectional area of that node section, represented by A_i, with a total of m nodes. In this allocation, each node's mass accounts for half of the mass section on its right side and half of the mass section on its left side. It's crucial to note that the root and tip sections' areas were halved before applying this weighted average. This adjustment is made to reflect that these two nodes contribute only one half, unlike the other nodes, where the root node lacks a more inner section, and the tip node lacks a more outer section.

For the vertical tail case, unlike the wing and horizontal tail (see Equation 4.3), the mass of the vertical tail was not divided by two.

In addition to the masses, the estimation and input of mass moments of inertia ($\boldsymbol{I}_{ji}$) for these masses are essential. Since the masses of these wing-like components are already distributed along the component span, only the mass moment of inertia along the component span is computed. The remaining mass moments of inertia are neglected.

For the fuselage case, the mass distribution spans across 11 nodes, extending from the nose of the fuselage to its aft most part in a straight line positioned at an altitude of 1.55 m from the reference point. To allocate the total estimated fuselage mass among these 11 nodes, a weighted average was employed, similar to the methodology used for wing-like components. This involved calculating the cross-sectional areas of the fuselage section, which were approximated to ellipses. The major and minor axes of these ellipses were determined based on the technical drawing (Figure 4.1.1) using reverse engineering techniques.

Regarding the mass moment of inertia of the fuselage, computations were limited to the mass moment of inertia along the fuselage's longitudinal axis for each fuselage node. The mass moments of inertia along the other two axes are already addressed through the mass distribution across the 11 fuselage nodes. Consequently, these additional mass moments of inertia do not need to be assigned to each individual fuselage node.

For the two mounted engines, the mass distribution methodology closely mirrored that employed for the fuselage. Each mounted engine, in this case, was characterized by only three nodes. The central node was strategically positioned based on assumptions about the component's center of mass, as derived from the technical drawing (Figure 4.1.1) and supported by DC-3 documentation [3, 25]. The remaining two nodes were located where the presumed centers of mass for the half sections of the mounted engine were anticipated.

To allocate masses, half of the total mass was assigned to the central node, while the remaining mass was distributed across the other two nodes in a manner that ensured a resultant moment of zero at node two. Regarding mass moments of inertia, consistent with the reasons explained in the fuselage case, calculations were limited to the mass moment of inertia along the longitudinal axis of the mounted engine.

Finally, the distribution of system masses is required. The components encompassed within the system masses include the landing gear, fuel system, flight control system, hydraulic system, avionics, electrical systems, air conditioning, and furnishings. The mass estimations for these diverse components were previously outlined, as detailed in Table 4.2.1. Now, the task at hand is to allocate these masses appropriately.

Concerning the landing gear, the total mass was partitioned among three locations, corresponding to the main landing gear and the rear landing gear. Precise information on the percentage distribution of the total mass for each location is documented in [15]. The positioning of these masses was easily derived from the technical drawing (Figure 4.1.1).

For the fuel system, the mass was distributed across two locations in each wing, symmetrically positioned in relation to the aircraft's symmetric plane and in proximity to the fuel tanks. The remaining masses were situated on the symmetric plane, accounting for the specifics of each component estimation as outlined in [15] and corroborated by the DC-3 documentation [3, 25]. These mass positions were adjusted to ensure alignment with the center of mass position of the aircraft, as documented in [25]. Figure 4.2.1 illustrates the mass modeling of the Douglas DC-3.

Grid points were not generated for the system masses; rather, these masses were linked to the fuselage or wing grid points, with offsets specified to account for the difference between the mass position and the grid points position.

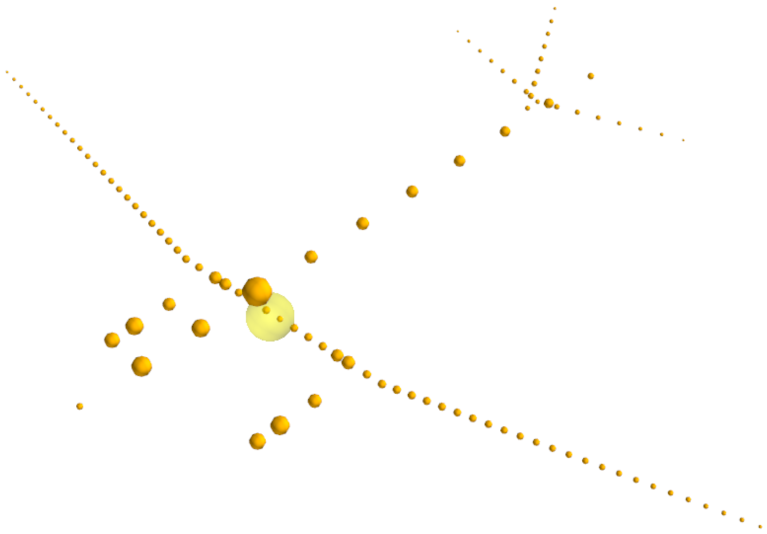

Figure 4.2.1: Douglas DC-3 mass modeling including structural, systems, crew and standard equipment masses.

4.2.3 Fuel Model

The modeling of fuel masses is more complex than that of other components. Due to the significant mass and inertia properties of the fuel, precise modeling is essential. Additionally, fuel levels can vary, necessitating a different approach for accurate representation. For that, the fuel masses need to be discretized per fuel bay, and modelled as volume elements to obtain inertia properties and filling levels. The fuel model was developed using the DLR in-house tool *ModGen*, necessitating the definition of fuel tank geometry. Initially, the fuel tanks were delimited between the front and rear spars, and from the first to the sixth rib, resulting in five fuel tanks per wing.

Additionally, a fuel density of 718.39 kg/m^3, corresponding to the aviation gasoline (Avgas) used, was sourced from [25]. Another crucial parameter is the utilization factor, which refers to the percentage of the tank's volume that is effectively filled with fuel, excluding the space occupied by fuel system components like pumps and lines. To ensure alignment between the model's mass of the full fuel tanks and the documented total mass in [25], a very small utilization factor was initially required with the configuration of five fuel tanks in each wing. However, having information about the total mass of the fuel when the tank is full, it became evident that the resultant model's mass was significantly larger with five fuel tanks. Consequently, a decision was made to reduce the number of fuel tanks in each wing from five to four (extending only until the fifth rib). This adjustment yielded a more reasonable utilization factor of 0.7864, bringing it into better alignment with industry standards and realities.

Finally, Z levels were defined based on the mass configuration. For example, a Z level of 1 was assigned for 100% fuel. Figure 4.2.2 illustrates the full fuel tanks model for the right wing.

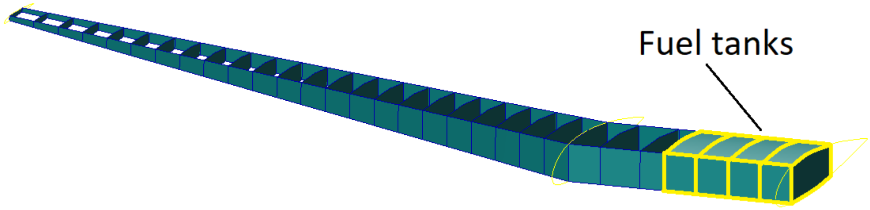

Figure 4.2.2: Douglas DC-3 right wing full fuel tanks.

4.3 Aerodynamics Model

For the aerodynamic modeling the DLM was employed. This method presupposes the construction of an aerodynamic mesh constituted by quadrilateral panels. While the DLM allows for modeling control surface motions, its accuracy in predicting control surface effects may be influenced by discretization, often necessitating empirical corrections [1]. This means that the meshing process has to be performed in a rigorous way. The aerodynamic mesh was obtained with the help of *ModGen*.

The wing's aerodynamic mesh comprises four macro panels. The first covers the inner section, the second spans the region between the wing kink and the beginning of the aileron section, the third is in front of the aileron section, and the fourth represents the aileron surface. Panel size in the chordwise direction must adhere to the condition $\Delta < 0.08V/f$ ($0.02V/f$ is needed for converged stability derivatives), where V is the minimum velocity, and f, in Hertz, is the maximum frequency to be analyzed. Another condition for panel geometry is that $AR < 4$ to ensure mesh quality, and an aspect ratio of $AR = 2$ was targeted [20].

The horizontal tail's aerodynamic mesh comprises three macro panels covering the region between the root and the beginning of the elevator section, in front of the elevator section, and representing the elevator surface. Similar conditions as those for the wing panels must be satisfied to ensure good mesh quality. Additionally, it is essential to align the wing and horizontal tail panels so that each wing panel corresponds to only one horizontal tail panel. Figure 4.3.1 shows the panel alignment and the macro panels highlighted in yellow.

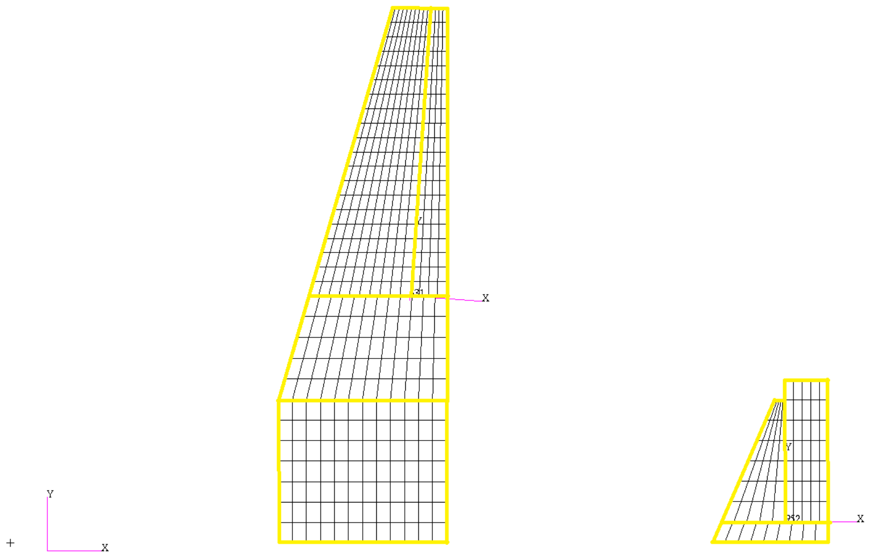

Figure 4.3.1: Aerodynamic mesh panels aligned between wing and horizontal tail.

While constructing the aerodynamic mesh for the horizontal tail, a concern arose in the second macro mesh near the tip where the aspect ratio of the panels exceeded the recommended limit of 4. Attempts were made to address this by increasing the number of divisions in the spanwise direction in that specific region. However, this adjustment led to alignment issues between the wing and horizontal tail panels. The final resolution involved chopping off this small problematic region near the tip, as illustrated in Figure 4.3.1. Given the relatively diminutive size of this extracted area, the impact on results is expected to be minor, and retaining the problematic situation would have introduced greater uncertainty into the results.

The aerodynamic mesh for the vertical tail comprises two macro panels. The first covers the region in front of the rudder section, while the second represents the rudder surface. Similar to the conditions mentioned earlier for the wing and horizontal tail cases, it is imperative to meet these criteria to ensure a high-quality mesh. Figure 4.3.2 displays the aerodynamic mesh for the Douglas DC-3 model.

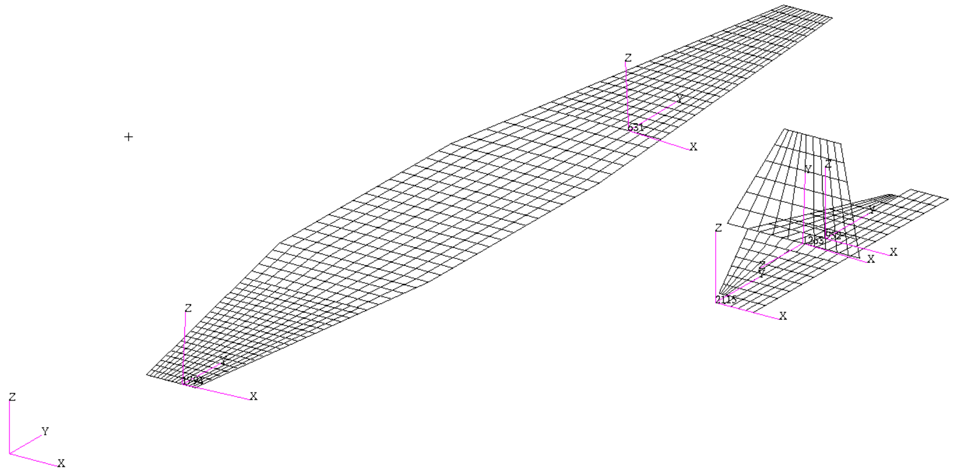

Figure 4.3.2: Douglas DC-3 model aerodynamic mesh.

While configuring the model for the left wing and left horizontal tail, adjustments were applied to the input files to guarantee that the local coordinate system's z-axis points upwards, for correct accounting of sweep and dihedral in the DLM. This alignment is evident in Figure 4.3.2.

4.4 Mass Configurations

Testing different mass configurations of an aircraft is integral to its development and certification process. Structural integrity is another key consideration, ensuring that the aircraft can handle the stresses imposed during flight and ground operations. Additionally, testing different configurations helps gauge fuel efficiency and range, as fuel consumption is influenced by total mass, including fuel load. Compliance with aviation regulations is crucial, and testing ensures the aircraft meets safety and performance standards set by regulatory authorities. Furthermore during the load, gust and flutter analyses, different mass cases need to be considered. Therefore, representative mass configurations were selected.

Mass configuration	Fuel	Payload	
M1	0%	0%	OEM
M2	100%	0%	Max Range
M3	49%	100%	MTOM
M4	0%	100%	-

Table 4.4.1: Mass configurations.

Taking this into account, four distinct mass configurations for the Douglas DC-3 have been outlined. The first configuration refers to the operational empty mass (OEM), covering only the weight of the structure, crew, and standard equipment. The second configuration denotes the maximum range, obtained by adding the maximum fuel capacity to the OEM. The third configuration represents the maximum take-off mass (MTOM), incorporating the maximum payload and the fuel capacity that constitutes 49% of the total fuel capacity. The fourth and final configuration encompasses the OEM along with the maximum capacity, excluding any fuel. Table 4.4.1 provides a summary of these four mass configurations.

Regarding payload specifics, the position and mass details were extracted from [25]. The payload is distributed across three compartments, as illustrated in Figure 4.4.1. The front compartment is situated 3.302 m from the datum point (the nose of the aircraft), the middle compartment at 8.128 m, and the rear compartment at 12.954 m from the datum point. According to the documentation [25], the front compartment can accommodate a maximum of 750 kg of payload, the middle compartment can hold up to 1543 kg, and the rear compartment has a maximum capacity of 227 kg.

A crucial piece of information from [25] is the center of gravity position for the aircraft in the first mass configuration (OEM) and the third mass configuration (MTOM). Consequently, by knowing the center of mass of the structures, crew, and standard equipment, and considering that the fuel model is generated using *ModGen* (extracting the center of gravity of the fuel from *ModGen*), adjustments were made to the center of gravity of the payload. This was done to align the center of gravity of the third configuration with the documentation, resulting in a slight modification in the distribution of payload mass across the three compartments.

Ultimately, 746 kg, 1543 kg, and 231 kg were allocated to the front, middle, and

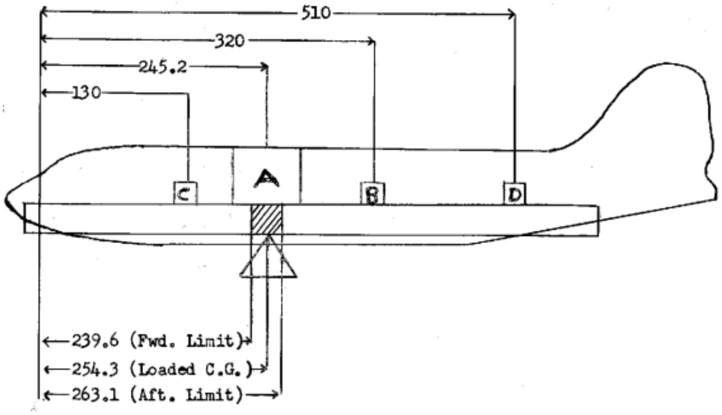

Figure 4.4.1: Payload compartments location, all units in inches [25].

rear compartments, respectively. Similar to the masses of other systems, these values were linked to fuselage grid points, each with its corresponding offsets.

Component	Mass [kg]
Payload (100%)	2520.00
Fuel (100%)	2625.80
Fuel (49%)	1289.65

Table 4.4.2: Masses of payload and fuel.

Table 4.4.2 presents the varied masses of payload and fuel utilized across the distinct mass configurations.

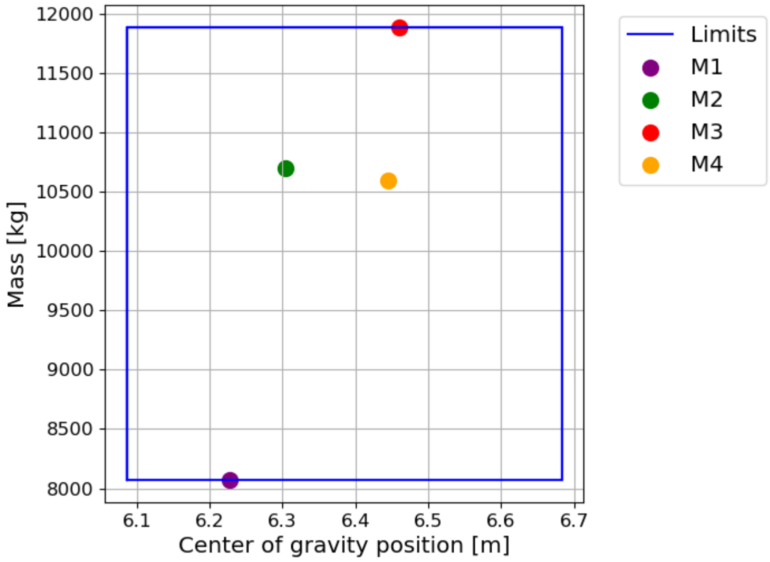

Figure 4.4.2: Mass against center of gravity position for the different mass configurations.

To ensure safety with regard to longitudinal stability and maneuverability, an acceptable range for the center of gravity was defined as per [25]. Figure 4.4.2 illustrates the relationship between the mass of various configurations and their respective center of gravity positions, along with the established limits for center of gravity and mass. It is evident that all four configurations are well within the specified limits. The center of gravity positions are measured from the aircraft's nose.

4.5 Modified Models

As previously mentioned, it was predicted that the original model would not fulfill the requirements established for the model. In this section the original model is going to be analysed, and the modified models are going to be presented and explained. To evaluate the models trim conditions are going to be studied. The trim case used to see the behaviour of the aeroelastic model encompassed horizontal level flight, a Load Factor of $n_Z = 1$, with a True Airspeed (TAS) of 70 m/s, and Flight Level FL000. The trim conditions for the Douglas DC-3 in the M3 mass configuration are outlined in Table 4.5.1. The M3 mass configuration was selected because it represents the scenario in which the aircraft undergoes the most significant structural deformations, thereby embodying a critical test case. For the original model, the determined values for the trim angle of attack and elevator deflection, $\alpha_{trim} = 1.39$ degrees and $\eta_{trim} = 0.83$ degrees respectively, appear reasonable. The lift coefficient $C_L = 0.423$, with elastic deformation contributing negatively by approximately 0.7%. Notably, this contribution is quite minor, indicating that the impact of aeroelasticity within this model is negligible.

Furthermore, Figure 4.5.1 illustrates the elastic deformation of the main wing under the previously mentioned trim conditions. It can be seen that the wing in the original model is bending upwards as expected. At the wing tip, the vertical displacement is $U_{flex,Z} = 0.13$ m and the elastic twist is $U_{flex,ry} = -0.14$ degrees. The wing leading edge is moving down and the wing trailing edge up. Once again, these values are notably small, underscoring the stiffness of the aeroelastic model. This outcome was expected, considering the era of the aircraft's original development and production in the 1930s, when understanding of aeroelasticity was limited. Consequently, aircraft designs leaned towards stiffness to prevent potential complexities and analysis challenges. That can be seen by the use of a big number of spars and ribs, compared with more modern aircraft in the same category.

Given that one of the primary objectives of this aeroelastic model is to underscore the significance of aeroelasticity in aircraft design, stability, flight control, and performance, modified versions of the original Douglas DC-3 aeroelastic model have been developed. Hence, four modified models were developed, and are going to be present next one by one.

In the first more flex model, alterations were made to the wing's stiffness and inertial properties. Regarding stiffness properties, the area moment of inertia about the chordwise axis ($I1$) was reduced to a values five times smaller, the moment of inertia about the axis perpendicular to the chordwise direction in the airfoil plane ($I2$), and torsional constant (J) were reduced by one order of magnitude. Additionally, the mass moments of inertia (I_{ji}) of the wing masses were increased by one order of magnitude. These modifications were applied in order to obtain higher deflections in terms of bending and torsion. Analysis of the trim results (Table 4.5.1) reveals that the contribution of elastic deformation to the lift coefficient has risen to 3.5% (More flex). Furthermore, elastic deformations are significantly more pronounced as depicted in Figure 4.5.1. Specifically, the vertical displacement at the wing tip measures $U_{flex,Z} = 0.64$ m, and the elastic twist amounts to $U_{flex,ry} = -0.62$ degrees. Consequently, it is evident that in this modified model, aeroelasticity assumes a much more prominent role, aligning with the intended objective.

	α_{trim} [deg]	η_{trim} [deg]	C_L	$C_{L_{cs}}$	C_{L_f}	C_{L_f}/C_L
Original	1.39	0.83	0.423	-0.008	-0.003	-0.7%
More Flex	1.52	0.90	0.423	-0.009	-0.015	-3.5%
More Flex 2	1.53	0.90	0.423	-0.009	-0.016	-3.8%
More Flex 3	1.60	1.10	0.423	-0.011	-0.020	-4.7%
More Flex 4	1.46	0.69	0.423	-0.007	-0.011	-2.6%

Table 4.5.1: Trim results for different aeroelastic models for M3.

Subsequently, to make sure that the variation in stiffness properties indeed accounts for the observed differences, a second modified aeroelastic model was crafted. This model retained the same stiffness modifications as the initial one but preserved the original inertia/mass properties. Examination of the trim results presented in Table 4.5.1 (More Flex 2) and the elastic deformation outcomes depicted in Figure 4.5.1 revealed striking similarities, corroborating the statement that stiffness properties are the pivotal factor. Notably, in this second modified model, the elastic twist registers a slightly larger magnitude at $U_{flex,ry} = -0.65$ degrees.

In order to explore the impact of the LRA position (and thus the loction of the elastic axis) on both trim results and elastic deformation, two additional modified aeroelastic models were constructed. In both cases, the wing stiffness properties remained consistent with those of the first and second modified models, while the inertial properties reverted to those of the original model, given their negligible influence.

In the third modified model, the wing LRA was shifted forward from a mid-position between the front and rear spars to a position 30% along the distance between them. Basically the elastic axis was positioned in front of the center of mass of the wing. Conversely, in the fourth modified model, the wing LRA was relocated aft, positioned at 70% along the distance between the front and rear spars. The elastic axis was positioned aft the center o mass. In both instances, the distribution of wing masses remained unchanged to ensure that the aircraft's center of gravity remained unaltered.

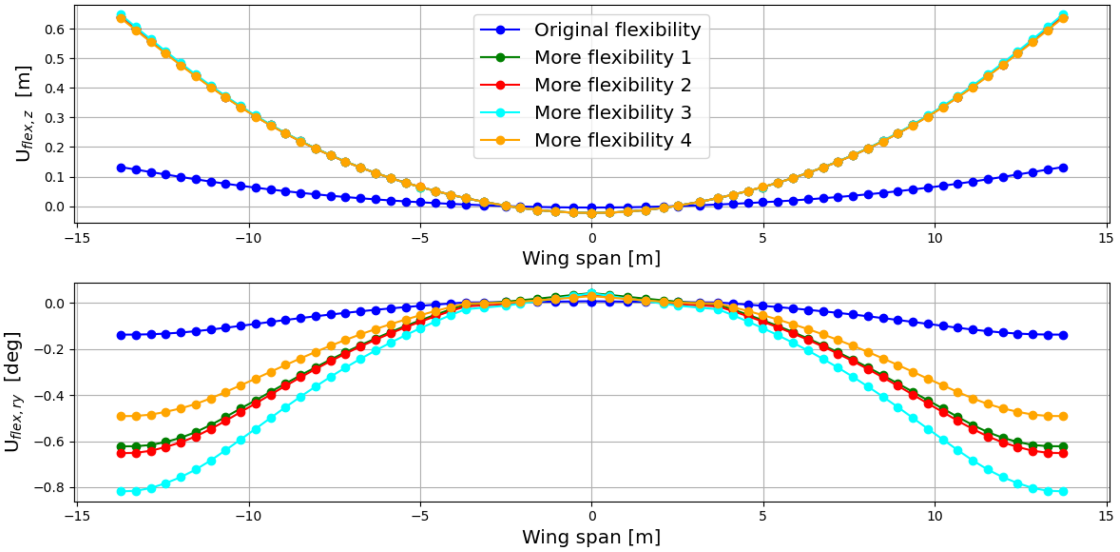

Figure 4.5.1: Elastic deformation of the main wing at Load Factor of $n_Z = 1$, with a True Airspeed (TAS) of 70 m/s, Flight Level FL000, and M3 mass configuration for the original and modified aeroelastic models.

Upon reviewing the results, it becomes evident that the elastic deformation contributes 4.7% to the lift coefficient in the third modified model and 2.6% in the fourth modified model. While the vertical displacements appear similar across both models, disparities emerge in the twist deformation. Specifically, the wing tip twist deformation measures $U_{flex,Z} = -0.82$ degrees for the third modified model and $U_{flex,Z} = -0.49$ for the fourth. Notably, the third modified model exhibits greater elastic deformations and a heightened contribution to the lift force, indicating that shifting the LRA forward amplifies aeroelastic effects. When the center of mass is behind the elastic axis, aerodynamic forces that cause wing deflection can lead to an enhancing moment. This moment can amplify the deflection because the inertia of the mass tends to follow the motion, Therefore, the third modified model, incorporating alterations in both stiffness properties and LRA position compared to the original aeroelastic model of the Douglas DC-3, effectively demonstrates the influence of aeroelasticity in trim level flight.

It's important to note that with the decrease in stiffness, the eigenfrequencies of these modified aeroelastic models have diminished, as anticipated. For example, the first flexible eigenfrequency has decreased to approximately 2-3 Hz, which is deemed acceptable as there is no interaction between the flexible modes and the rigid body modes.

A fundamental requirement of this aeroelastic model is the presence of a distinct flutter mechanism, where bending and torsion modes are coupled, occurring at velocities beyond the flight envelope but within the subsonic regime (Ma<0.6). Upon examining the flutter mechanism and velocity using both *MSC Nastran* and *Loads Kernel*, it was noted that the flutter speed was well within the transonic regime.

As a result, adjustments were necessary for this third modified model. Regarding stiffness properties, the area moment of inertia about the chordwise axis ($I1$) remained unchanged, while the moment of inertia about the axis perpendicular to the chordwise direction in the airfoil plane ($I2$) and the torsional constant (J) were halved compared to the previous modified model. This adjustment aimed to enhance twist deformations, thereby enhancing the coupling between bending and torsion modes. Additionally, the distribution of wing masses was changed. Previously concentrated in the LRA, the masses were relocated towards the trailing edge, while the LRA itself was shifted forward from its original position, which was 30% between the front and rear spars, to a new position, 20% along the distance between them. The wing masses were then positioned 45% of the wing section chord aft of the LRA. Furthermore, a redistribution of wing mass was carried out, with mass being transferred from nodes in sections near the wingtip to nodes in sections closer to the wing root.

These modifications led to a notable reduction in flutter speed, achieving a flutter phenomenon within the subsonic regime, featuring a distinct coupling between bending and torsion modes as intended. The rationale behind these adjustments to mass distribution are: first, to facilitate the observation of the flutter mechanism with coupling between bending and torsion modes by shifting masses aft and the LRA forward; second, by moving some wing mass closer to the root, the weight distribution towards the wingtip decreases, so the aerodynamic forces needed to counteract the weight force at the tip decreases, necessitating a lower dynamic pressure, and consequently, a lower velocity to induce flutter. The mechanisms described above allowed the flutter speed to drop significantly while staying outside the flight envelope. The flutter check is presented and discussed in detail in section 5.4.

4.6 Eigenmodes

Having obtained the final aeroelastic model eigenmodes and eigenfreqeuncies can be computed. For that, *Loads Kernel* was used. The same calculations can be performed in *MSC Nastran* with the help of solution sequence SOL103. For the visualization of the eigenmodes *Model Viewer* was utilized.

Looking at the *Loads Kernel* results for the final modified aeroelastic model, the first six eigenvalues, as expected, are approximately 0 Hz (in the order of magnitude of 10^{-5} and 10^{-6} Hz]. These eigenvalues correspond to the rigid body modes. In Figure 4.6.1 the first four flexible mode shapes for the unconstrained aircraft in vacuum for the M3 mass configuration are shown. It can be seen, that the first eigenmode has a eigenfrequency of 3.17 Hz which does not fall in the range expected from an aircraft of the size and weight of the Douglas DC-3, as well as the design and manufacture techniques of that time. This was expected since the model was tuned significantly. One observation that is noticeable is that there is a mode correspondent to a pure wing torsion at f=9.60 Hz, which is the seventh eigenmode. This was something that was aimed to have. In several modes the wing bending is coupled with the wing torsion as expected.

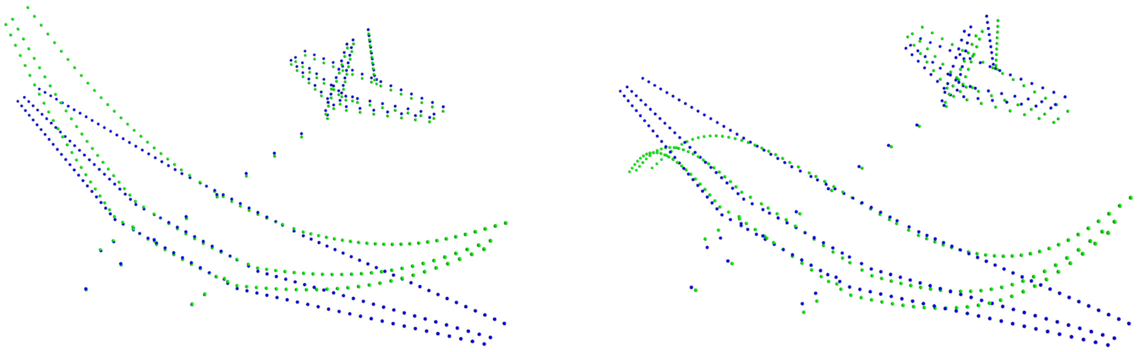

(a) Mode 1, first symmetric wing bending, f=3.17 Hz

(b) Mode 2, first antisymmetric wing bending, f=4.72 Hz

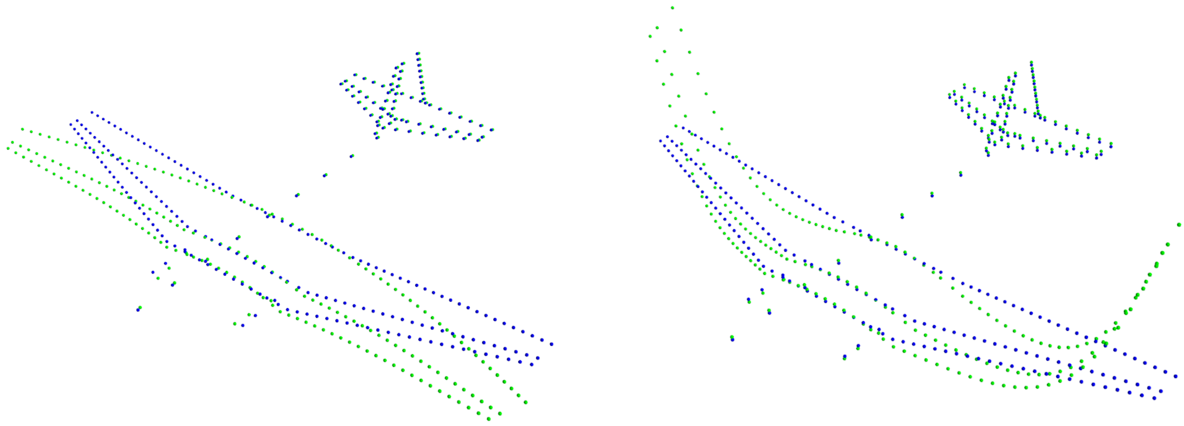

(c) Mode 3, first symmetric in-plane wing bending, f=7.26 Hz

(d) Mode 4, second symmetric wing bending, f=8.00 Hz

Figure 4.6.1: First four flexible mode shapes, M3.

Chapter 5

Results

With the aeroelastic model of the final modified configuration developed in Chapter Four, various analyses can now be performed to compare and demonstrate the capabilities of both *Loads Kernel* and *MSC Nastran*. These analyses include trim analyses, maneuver and gust load analyses, and flutter checks. Moreover, the determining role of aeroelasticity is showed in the different simulations.

5.1 Trim Cases

Using the mass and stiffness matrix obtained in *MSC Nastran*, the trim conditions for the Douglas DC-3 model were computed. This calculation was done using the DLR in-house software *Loads Kernel*, as well in *MSC Nastran* using *SOL 144*.

Three trim cases were performed at True Airspeed (TAS) of 70 m/s and Flight Level FL000. This trim velocity was chosen because is roughly the middle point between the maneuvering speed V_A = 113 KEAS = 58.13 m/s and the design speed for maximum gust intensity V_B = 170 KEAS = 87.46 m/s. The first case corresponds to a horizontal level flight, a Load Factor of n_Z = 1; the second one to a push-down maneuver, a Load Factor of n_Z = -1; and the third one to a pull-up maneuver, a Load Factor of n_Z = 2.5. These load cases where chosen having in consideration the flight envelope that was obtained using the CS-25 [11], which refers to the certification specifications established by the European Union Aviation Safety Agency (EASA) for the airworthiness of large airplanes.

Upon examining the trim results, several notable conclusions emerge. Table

5.1.1 presents the α_{trim} outcomes for the final modified model, revealing values that comfortably align within the acceptable range for both the rigid and flexible versions across both software programs. Comparing the results between both software it can be seen that they match quiet well, having just very small differences. To understand the sources of these small differences is important to discuss the differences between both software. While the simulation performed in *Loads Kernel* uses a modal approach, the SOL 144 performed in *MSC Nastran* it is not. Hence, for the *Loads Kernel* case a convergence study had to be performed. For that, the number of eigenmodes truncated were progressively increased until the trim results converged. At the end, it was concluded that a total number of 71 eigenmodes is enough to obtain convergence. On top of that, *MSC Nastran* considers the elastic deformation on the wing root to be null, while *Loads Kernel* allows the wing root to have elastic deformation. This makes the comparison not so direct in the flexible case. For instance, in order to compare the α_{trim} flexible results, in the *Loads Kernel* results for α_{trim} the ”elastic incidence angle” (basically, the wing root elastic twist deformation) was subtracted.

Comparative analysis between the rigid and flexible aircraft configurations reveals evident disparities. Notably, when comparing the *Loads Kernel* α_{trim} results for horizontal level flight, a significant 26.6% difference emerges, underscoring the pronounced impact of aeroelasticity in aircraft design. This underscores the imperative of considering aeroelasticity into flight performance, stability, and control analyses.

	Loads Kernel		**Nastran SOL144**	
	Rigid	**Flexible**	**Rigid**	**Flexible**
n_Z=1	1.275 deg	1.614 deg	1.271 deg	1.639 deg
n_Z=-1	-8.656 deg	-8.823 deg	-8.626 deg	-8.845 deg
n_Z=2.5	8.732 deg	9.517 deg	8.694 deg	9.502 deg

Table 5.1.1: Trim cases α_{trim} results for the final modified model, for M3.

Similarly, Table 5.1.2 showcases the η_{trim} findings, depicting elevator deflections well within a reasonable and realistic spectrum, considering the established range for elevator trim-tab deflections from 10.2 degrees (nose down) to -11.4 degrees (nose up) [3]. Again, the results between the *Loads Kernel* and *MSC Nastran* are very similar, and the results between flexible and rigid cases show significant differences meeting the α_{trim} results.

Further elucidating the significance of aeroelasticity, Table 5.1.3 shows the $\frac{C_{L_f}}{C_L}$

	Loads Kernel		Nastran SOL144	
	Rigid	**Flexible**	**Rigid**	**Flexible**
$\mathbf{n_Z}$**=1**	0.076 deg	0.241 deg	0.074 deg	0.237 deg
$\mathbf{n_Z}$**=-1**	-7.632 deg	-7.687 deg	-7.635 deg	-7.691 deg
$\mathbf{n_Z}$**=2.5**	5.857 deg	6.209 deg	5.855 deg	6.183 deg

Table 5.1.2: Trim cases η_{trim} results for the final modified model, for M3.

results obtained with *Loads Kernel*, highlighting the contribution of aircraft flexibility to total lift. For instance, in horizontal level flight, flexibility contributes a detrimental -5.22%. This negative contribution is explained analysing the elastic deformations of the main wing at these trim cases, as is going to be shown further on.

	Loads Kernel	
	Rigid	**Flexible**
$\mathbf{n_Z}$**=1**	0	-5.22%
$\mathbf{n_Z}$**=-1**	0	-2.03%
$\mathbf{n_Z}$**=2.5**	0	-4.77%

Table 5.1.3: Trim cases $\frac{C_{L_f}}{C_L}$ results for the final modified model, for M3.

Moreover, to compare in more detail both software trim results, in Tables 5.1.4 and 5.1.5, the elastic tip vertical displacement $U_{flex,Z_{tip}}$ and the elastic tip twist $U_{flex,ry_{tip}}$, respectively, are exposed. Obviously, for the rigid cases all the elastic deflections are null. In the elastic case the results of both software are in accordance. The small differences on these results meet the small differences encountered in the α_{trim} and η_{trim} results.

	Loads Kernel		Nastran SOL144	
	Rigid	**Flexible**	**Rigid**	**Flexible**
$\mathbf{n_Z}$**=1**	0	0.641 m	0	0.684 m
$\mathbf{n_Z}$**=-1**	0	-0.619 m	0	-0.628 m
$\mathbf{n_Z}$**=2.5**	0	1.636 m	0	1.668 m

Table 5.1.4: Trim cases $U_{flex,Z_{tip}}$ results for the final modified model, for M3.

To understand the influence of elasticity on aircraft performance, stability, and control, the main wing's elastic deformations along the span is illustrated in Figure 5.1.1 across the different trim cases are analyzed.

Elastic vertical displacement $U_{flex,Z}$ along the wing span reveals upward bending during horizontal level flight and pull-up maneuvers, and downward bending during

	Loads Kernel		Nastran SOL144	
	Rigid	**Flexible**	**Rigid**	**Flexible**
n_Z=1	0	-0.994 deg	0	-0.944 deg
n_Z=-1	0	0.600 deg	0	0.599 deg
n_Z=2.5	0	-2.179 deg	0	-2.101 deg

Table 5.1.5: Trim cases $U_{flex,ry_{tip}}$ results for the final modified model, for M3.

push-down maneuvers. This alignment is expected, as lift force in the former cases lifts the wing, while in the latter, it pushes it downward.

Notably, during pull-up maneuvers, the most pronounced vertical displacements occur, particularly at the wing tip, reaching $U_{flex,Z} = 1.55$ m, equivalent to 10.7% of the half wing span. This displacement remains within the accepted range for linear elasticity assumptions applied in these analyses, typically valid until 12-15% of the tip's vertical displacement relative to half the wing span.

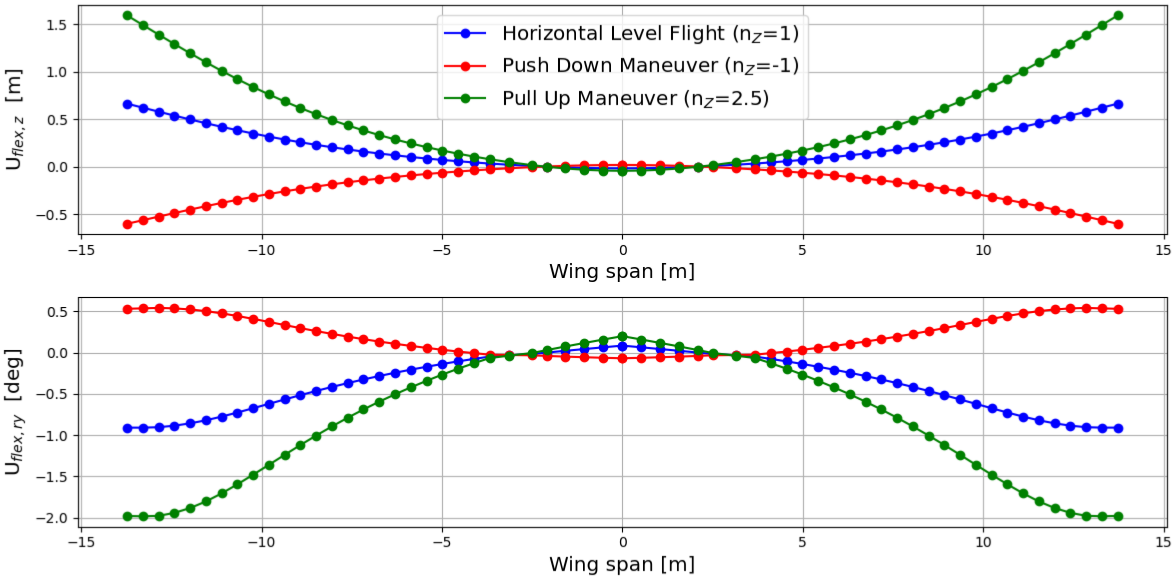

Figure 5.1.1: *Loads Kernel* elastic deformation of the main wing at certain speed, M3 for the final modified aeroelastic model.

Evaluating elastic twist $U_{flex,ry}$ along the wing span, a nose-down torsional twist is observed during horizontal level flight and pull-up maneuvers in the outer wing section, indicating negative twist values. At the inner section a nose-up torsional twist is observed, but with very small values compared with the outer section. On the opposite, during push-down maneuvers, the opposite trend is evident. Notably, the most significant elastic twist occurs at the wing tip during pull-up maneuvers, with a value of $U_{flex,ry} = -1.98$ degrees. This substantial twist significantly influences lift distribution along the wing, hence affecting overall wing performance.

5.2 Maneuver Loads

Maneuver loads are important to analyse because they are typically a driving factor for the sizing of the aircraft primary structure. For the selection of loads cases, CS-25 was used as reference. The three maneuvers used for the trim cases were used, so the horizontal level flight (n_Z = 1), the push-down maneuver (n_Z = -1) and the pull-up maneuver (n_Z = 2.5). Additionally, two roll maneuvers were added. From CS-25 Amendment 28 [11], the aircraft at trim with a 30° bank angle has to be able to roll to a 30° bank angle in the other direction in no more than 11 seconds. That corresponds to a roll velocity of p = 5.45 °/s. A roll velocity of p = 5.45 °/s is actually quiet slow and it does not produce very interesting results in the maneuver loads. For that reason, this roll maneuver is going to be performed in 3 seconds rather than 11. Hence, a roll velocity of p = 20 °/s. All these maneuvers were performed at True Airspeed (TAS) of 70 m/s and Flight Level FL000.

The resulting nodal loads were integrated at designated monitoring stations along the wing span (Figure 5.2.1) to derive section loads, utilizing the *Loads Kernel*. In this section only the *Loads Kernel* results are analysed, since in the previous section the similarity between *MSC Nastran* and *Loads Kernel* was proved. A total of 16 monitoring stations were strategically placed on each wing. Key quantities of interest for the wing include the bending moment M_x, torsional moment M_y, and shear force F_z.

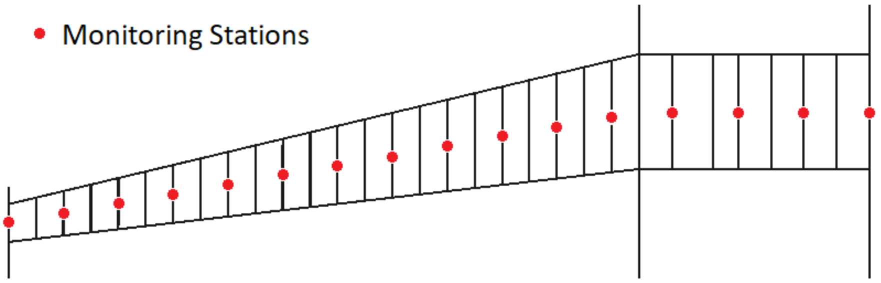

Figure 5.2.1: Monitoring stations location on the left wing.

One-dimensional envelopes along the wing span provide insights into the evolution of section loads across the wing, with each red dot denoting the highest positive and negative bending moment at each monitoring station. Figure 5.2.2 illustrates the envelope of the bending moment M_x along the wing span. A comparison between the results for the right and left wings reveals symmetrical bending moments with reversed signs, attributable to the rearward orientation of the x-axis in the coordinate system for both sides.

In the left wing, the most significant negative bending moment arises from the pull-up maneuver with a load factor of n_Z=2.5. Conversely, the largest positive bending moment stems from the push-down maneuver with a load factor of n_Z=-1. Hence, a negative sign denotes an upward bending moment, while a positive sign indicates a downward bending moment. Conversely, for the right wing, the opposite occurs due to the definition of the x-axis. This outcome aligns with expectations, as the pull-up maneuver induces upward wing bending, while the push-down maneuver leads to downward bending. The highest bending moments M_x are at the root as expected.

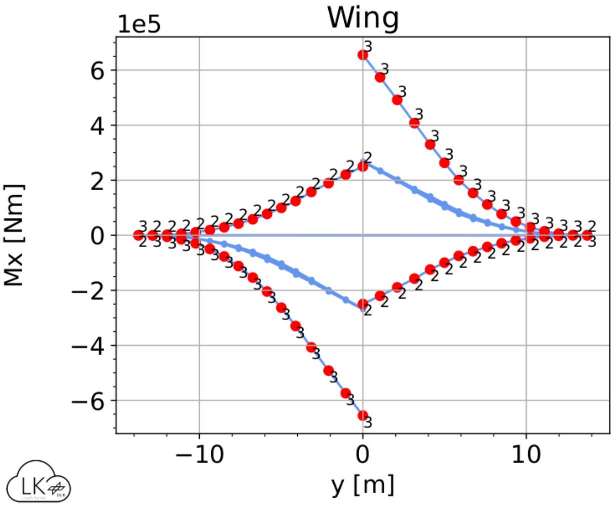

Figure 5.2.2: Bending moment M_x along the wing span.

Figure 5.2.3 depicts the envelope of the torsional moment M_y along the wing span. Notably, the y-axis of the coordinate system points towards the right for both the right and left wings.

In the inner section of the wing, the most significant negative torsional moments M_y stem from the pull-up maneuver, while the highest positive torsional moments M_y in the inner section result from the push-down maneuver. In the outer section of the wing closer to the kink the highest negative torsional moments M_y arise from the push-down maneuver. Conversely, the highest positive torsional moments M_y are induced by the pull-up maneuver.

These observations can be elucidated by recalling the elastic twist deformation along the wing span in Figure 5.1.1. A nose-down torsional twist is evident during pull-up maneuvers in the outer wing section, resulting in a positive torsional moment. Conversely, in the inner section, a nose-up torsional twist is observed, yielding a negative torsional moment. The opposite phenomenon occurs during the push-down maneuver.

For the rest of the outboard section of the wing, the maneuver loads are defined by the roll maneuvers. The positive and negative torsional moments M_y peaks are located in the third monitoring station, which is located in the inboard section of the wing close to the kink.

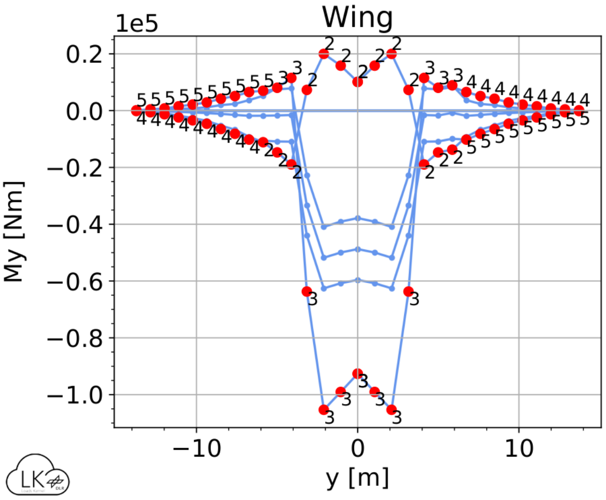

Figure 5.2.3: Torsional moment M_y along the wing span.

Figure 5.2.4 illustrates the envelope of the shear force F_z along the wing span. Notably, the z-axis of the coordinate system points upwards for both the right and left wings, implying that a positive sign denotes a shear force directed upwards for both sides.

The most substantial positive shear force arises from the pull-up maneuver, while the largest negative shear force results from the push-down maneuver. This observation aligns with the explanation provided for the bending moment. The positive and negative shear force F_z peaks are located in the fourth monitoring station, which is located in the inboard section of the wing close to the kink.

Comparing the results for the right and left wings, the overall trends and magnitudes of the shear forces are consistent, as expected from the symmetrical nature of the aircraft design and maneuvers.

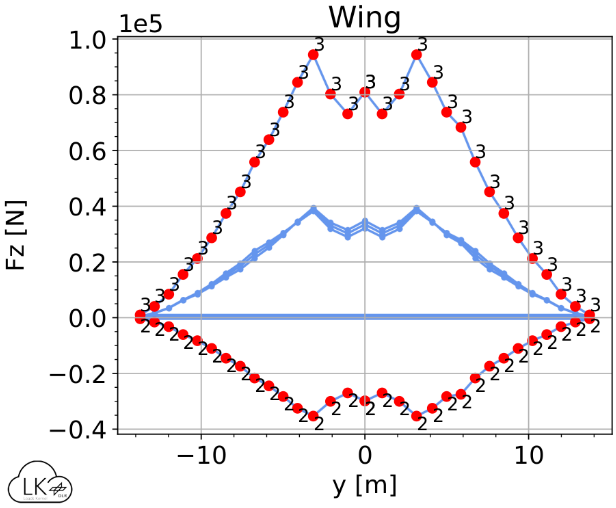

Figure 5.2.4: Shear force F_z along the wing span.

Moreover, to identify the critical load cases, two-dimensional load envelopes were constructed, illustrating combinations of two significant section loads. For the wing, the pertinent load envelopes are F_z/M_x and M_x/M_y. But only the M_x/M_y load envelope is going to be analysed. Given the wing's configuration with an outboard section featuring sweep and a rectangular inboard section, section loads were computed in the global coordinate system (x-y-z directions: aft-right-up) for the inboard section, and in a local coordinate system for the outboard section.

For instance, Figure 5.2.5 illustrates the load envelope detailing the torsional moment M_y and bending moment M_x at the left wing root. It is evident that the most significant negative bending moment M_x aligns with the pull-up maneuver, while the highest positive bending moment M_x corresponds to the push-down maneuver. Similarly, regarding the torsional moment M_y, the peak negative torsional moment M_y coincides with the pull-up maneuver, and the maximum positive torsional moment M_y aligns with the push-down maneuver.

Furthermore, it's noticeable that the roll maneuvers exhibit identical bending moments M_x to horizontal level flight since the load factor remains constant at $n_Z = 1$ for all three maneuvers. However, in terms of the torsional moment M_y, the roll maneuvers display an offset (one for each side) compared to horizontal level flight. This outcome was anticipated as the roll maneuver involves aileron deflection, contributing to an increase in elastic wing twist.

When examining the load envelope detailing the torsional moment M_y and bending moment M_x at the wing kink (Figure 5.2.6), notable differences emerge. The limit

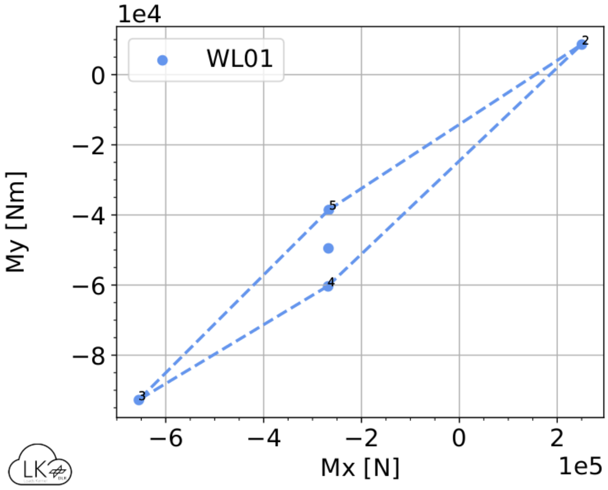

Figure 5.2.5: Bending moment M_x and torsional moment M_y at the wing root.

values for the bending moment M_x correspond to the same maneuver cases. However, for the torsional moment M_y, the highest negative torsional moment M_y aligns with the push-down maneuver, while the highest positive torsional moment M_y corresponds to the pull-up maneuver. This discrepancy stems from the observation made in the previous section (Figure 5.1.1), where the elastic twist $U_{flex,ry}$ of the outboard wing section after the kink becomes negative (nose-down torsional twist), thus causing this shift compared to results from the inboard wing section at the wing root.

Furthermore, the roll maneuvers exhibit a distinct offset (one for each side) compared to horizontal level flight, transforming the shape of the envelope from an elongated rhombus to a bulkier one.

Moreover, it's evident that while the magnitude of the bending moment M_x remains consistent, the limit values at the wing kink are slightly smaller compared to those at the wing root. This holds true for the torsional moment M_y as well. The wing root experiences the highest torsional and bending moments due to its location at the junction of the wing and fuselage, where aerodynamic forces are concentrated and transmitted. Additionally, structural loads from maneuvers are typically greatest at this point due to the leverage effect of the wing's length and its attachment to the fuselage.

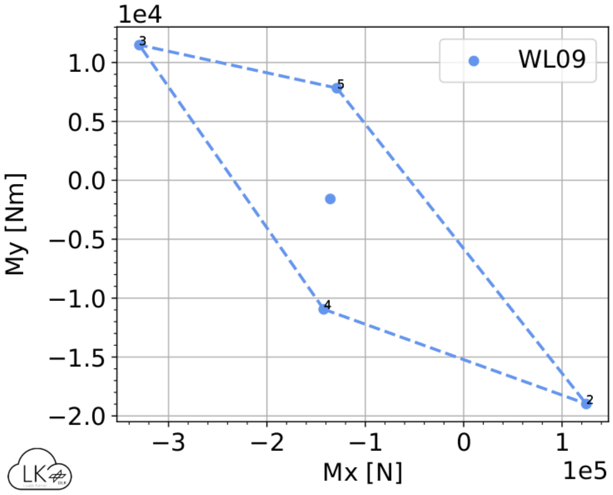

Figure 5.2.6: Bending moment M_x and torsional moment M_y right after the wing kink.

5.3 Gust Loads

To study the gust loads the (1-cos) Discrete Gust Model is used in *Loads Kernel*. The gust analyses was performed in the same conditions as the maneuvers at True Airspeed (TAS) of 70 m/s and Flight Level FL000 at trim conditions. In accordance to CS-25.341 [11] the gust profiles at sea level were obtained, and are presented in Figure 5.3.1. To have a more detailed understanding of the gust shapes, the gust gradients and their corresponding peak velocities are listed in Table 5.3.1. The different gust gradients were selected so that the spectrum required from the certification specifications was covered, and the forces/moments peaks in the plots over time was correctly captured. Concerning the orientation of the gust, only vertical gusts are going to be studied.

Gust gradient [m]	**9**	**16**	**23**	**30**	**37**	**51**	**65**	**79**	**93**	**107**
Peak velocity [m/s]	10.4	11.4	12.1	12.7	13.1	13.8	14.4	14.9	15.3	15.6

Table 5.3.1: Gust gradients and corresponding peak velocities shown in Figure 5.3.1.

Once again, one-dimensional envelopes along the wing span were studied to provide insights into the evolution of section loads across the wing.

Figure 5.3.2 illustrates the envelope of the bending moment M_x along the wing span. Comparing the results between the maneuver (Figure 5.2.2) and gust loads, one can see that magnitude of the values is the same. Due to the fact that the results are symmetric, the conclusions drawn from the right wing (y>0) are valid for the left wing.

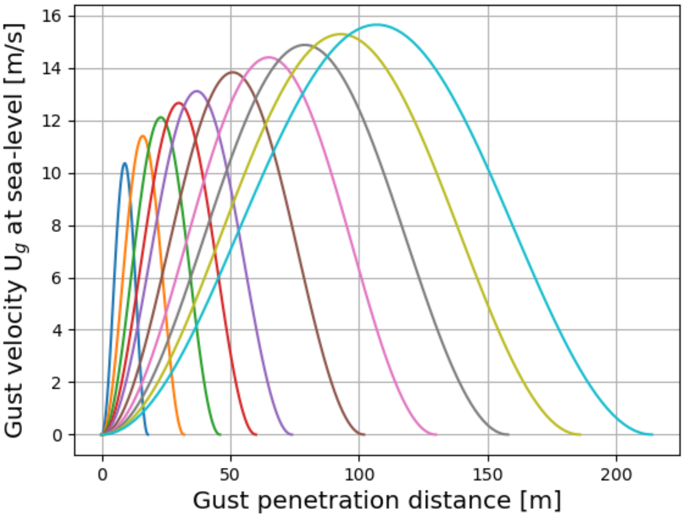

Figure 5.3.1: Gust shapes at sea-level according to CS-25.

In the inboard part of the right wing, the highest positive bending moment arise from the gust load with gust gradient $H = 23$ m. For the outboard section the highest values correspond to the gust load with gust gradient $H = 16$ m, except for the last three monitoring stations closer to the tip. For the monitoring station located at the tip the highest value is for the gust load with gust gradient $H = 51$ m and for the other two is for the gust load with gust gradient $H = 9$ m. On the other hand, the highest negative bending moment arises from the gust load with gust gradient $H = 51$ m for the entire wing span, except for the tip for which the highest value is for the gust load with gust gradient $H = 37$ m.

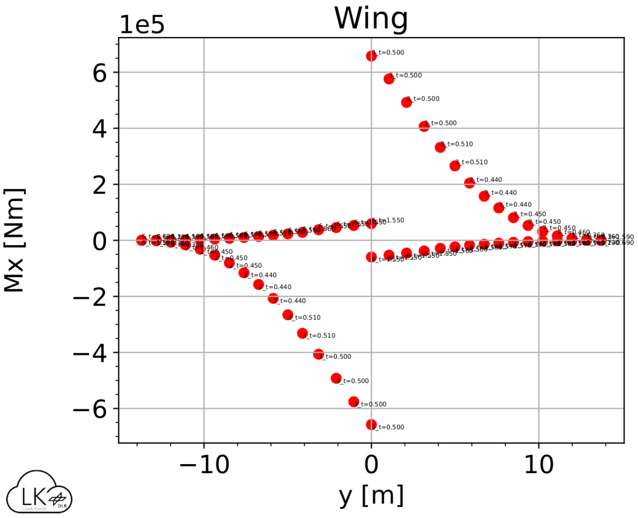

Figure 5.3.2: Bending moment M_x along the wing span.

Figure 5.3.3 depicts the envelope of the torsional moment M_y along the wing span. A comparison between the results for the maneuver (Figure 5.2.3) and gust loads shows that once again the magnitude of the values is the same.

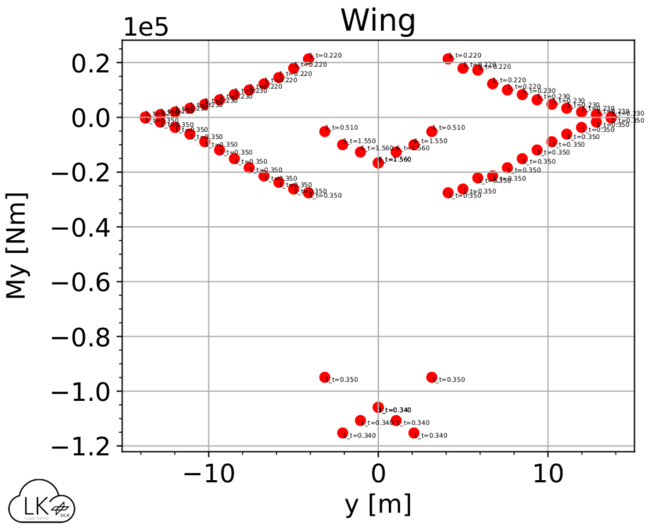

Figure 5.3.3: Torsional moment M_y along the wing span.

Analysing Figure 5.3.3, the most significant negative torsional moments M_y stem from the gust load with gust gradient H = 9 m at the time instance of 0.350 s, except for the most inner monitoring stations which correspond to the time instance of 0.340 s. The highest positive torsional moments M_y arise from the the gust load with gust gradient H = 9 m too at time instance between 0.220 s and 0.230 s, except for the three most inner monitoring station, which actually have still a negative torsional moment M_y and correspond to the gust load with gust gradient H = 51 m.

Figure 5.3.4 illustrates the envelope of the shear F_z along the wing span. Again, the magnitude of the loads is similar to the one of the maneuver loads (Figure 5.2.4).

For the entire wing span, the highest negative shear forces arise from the gust load with gust gradient H = 51 m, similar to what happen for the bending moment envelope. The highest positive shear forces come from the gust load with gust gradient H = 23 m, except for the six most outer monitoring station, which come from the gust load with gust gradient H = 16 m. Again, a behaviour similar to the one observed for the bending moment envelope.

As it was done for the analyses of the maneuver loads, two-dimensional load envelopes were constructed. Again, the M_x/M_y load envelope is going to be interpreted. In Figure 5.3.5 the torsional and bending moments envelope is shown

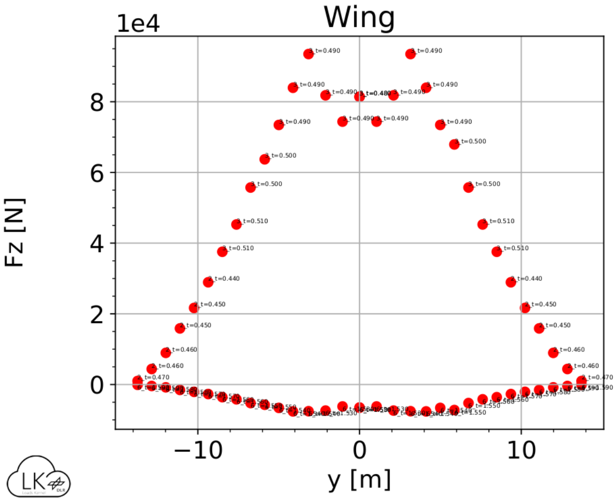

Figure 5.3.4: Shear force F_z along the wing span.

for the left wing root. First, one can see that the envelope shape resembles a certain direct correlation between the bending and torsional moments. Second, one can see that the highest negative bending moments M_x are reached by the gust loads with gust gradients $H = 16, 23, 30$ and 37 m (the different gust loads are identified in Figure 5.3.5 using numbers), while the highest negative torsional moments M_y are reached by the gust loads with gust gradient $H = 9$ m. The highest positive bending moments M_x are reached by the gust load with gust gradient $H = 51$ m, this gust load corresponds to the smallest negative torsional moments M_y. Third, both maneuver and gust envelopes are very close to each other, which is an indicator for well-selected load cases which harmonize with each other in the sense that there are no extreme loads cases which dominate the design. That can be concluded comparing Figures 5.2.5 and 5.3.5. The greater number of data points in the gust load results compared to the maneuver load results can be attributed to the concept of time slices. In the case of gust loads, multiple time instants are analyzed, generating a point for each instant in each gust load scenario. This leads to a higher density of data points in the gust load results.

When examining the gust load envelope detailing the bending moment M_x and torsional moment M_y at the wing kink (Figure 5.3.6), notable differences arise. First, one can see that the envelope as a more rounded shape, which indicate that there is not a direct correlation between the bending and torsional moments. The same change in the envelope shape occurred when analysing the maneuver loads showing the harmonization between maneuver and gust loads (Figures 5.2.6 and 5.3.6). Second, torsional moment M_y have positive values. Third, the highest negative bending

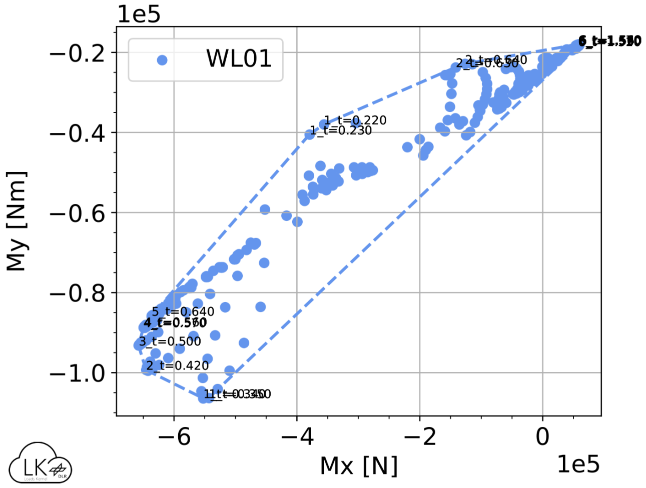

Figure 5.3.5: Bending moment M_x and torsional moment M_y at the wing root.

moments M_x are reached again by the gust loads with gust gradients H = 16, 23, 30 and 37 m but the peak as a smaller value compared to the wing root envelope. The highest negative torsional moments M_y are reached again by the gust loads with gust gradient H = 9 m, but this time with a value a order of magnitude higher. The highest positive bending moments M_x are reached by the gust load with gust gradient H = 37, 51 and 65 m with approximately the same values as in the wing root case. Now, the highest positive torsional moment M_y is reached by the gust loads with gust gradient H = 9 m.

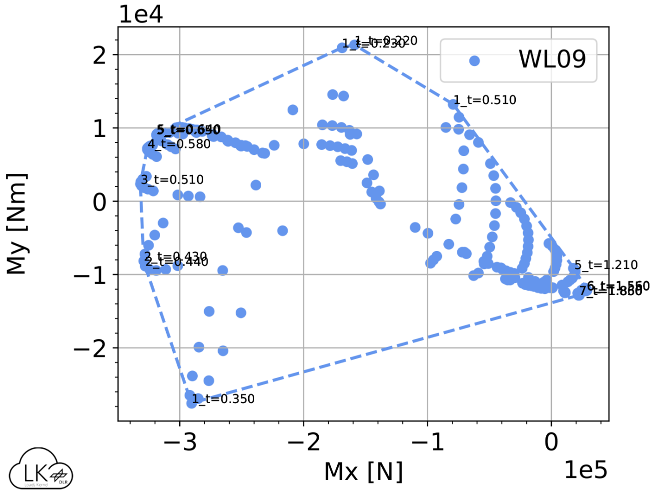

Figure 5.3.6: Bending moment M_x and torsional moment M_y right after the wing kink.

Furthermore, in order to have a deeper understanding of the gust loads, the forces and moments of the different gust profiles were plotted over time. The time step is variable to accurately capture the transient nature of gust loads, and the results are outputted every 0.01 seconds. It maintains acceptable results and at the same time is large enough to not be very computationally demanding. The interval time selected for the gust analyses was 3 seconds, which is more than enough to capture the several peaks for each gust profile.

Observing, the bending moments M_x over time for the different gust gradients at the right wing root (Figure 5.3.7a), it can be seen that the magnitude of the positive peaks is very close to the negative peaks, which was unexpected. Moreover, the highest positive peak is reached for a gust gradient of H = 23 m. Empirical data collected in the 1940s shows that the highest gust excitations on legacy aircraft occur at a gradient corresponding to 12.5 spatial chord lengths on average [13]. Being the mean aerodynamic chord $\bar{c}$ = 3.508 m, the highest positive peak should have been reached around a gust gradient of H = 44 m, almost doubled the value obtained.

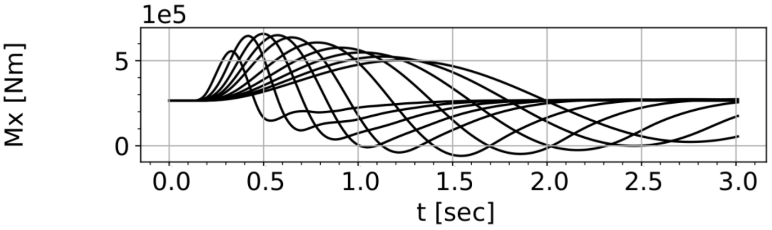

(a) Wing root.

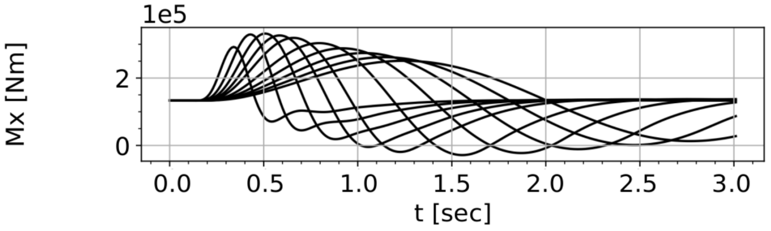

(b) Wing kink.

Figure 5.3.7: Bending moment M_x over time for different gust gradients.

Concerning the shear force F_z over time plots, the same conclusions can be drawn, as can be seen in Figure 5.3.8a.

Moving to the torsional moment M_y over time for different gust gradients (Figure 5.3.9a) at the wing root, the negative peaks are bigger than the positive and the highest negative peak arises from the gust gradient of H = 9 m, the smallest gust gradient. Again, different than the expected.

When moving to the wing kink section, it can be noticed than in the torsional moment M_y plot over time plot (Figure 5.3.9b) for the gust gradient of H = 9 m

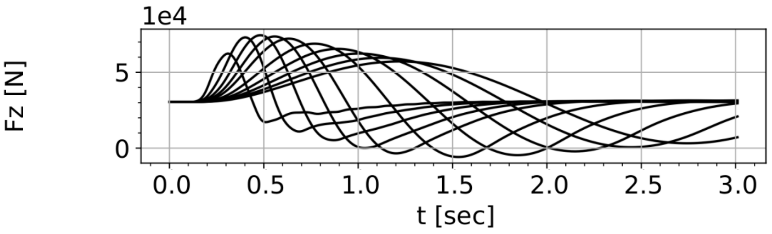

(a) Wing root.

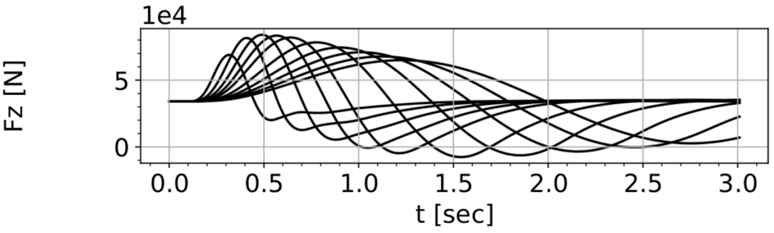

(b) Wing kink.

Figure 5.3.8: Shear force F_z over time for different gust gradients.

oscillations with big amplitude appear. The justification for this behaviour can be the excitation of one eigenmode. The frequency of these oscillations is around 3.3 Hz, which is very close to the eigenfrequency of the first symmetric wing bending mode f = 3.17 Hz. This means that most probably this mode is being excited by the gust with the gust gradient of H = 9 m. But, these oscillations are seen in the torsional moment M_y plot. The possible justification for that is the torsional stiffness is much lower compared to the bending stiffness, and on top of that the wing mass points are located far aft of the LRA, which creates a strong bending and torsional coupling. In the bending moment M_x and shear force F_z over time plots in the wing kink section (Figures 5.3.7b and 5.3.8b) no considerable changes are visible compared with the plots on the wing root.

In order to get to the sources of these unexpected results: the negative and positive peaks having the same size and the highest peak not correspond to the gust gradient expected, some extra simulations were performed. It was discovered a coupling between the gusts and one of the longitudinal flight mechanics modes, the short period. One way to eliminate this coupling is to decreased the distance between the aerodynamic center and the center of gravity, so the static margin. The aircraft model has a very high static margin in the M3 mass configuration, which was reduced to approximately 10%. This resulted in the magnitude of the positive and negative peaks of the moments/forces over time plots to change so that the magnitude of these positive and negative peaks was then much different between them. On top of that, the highest

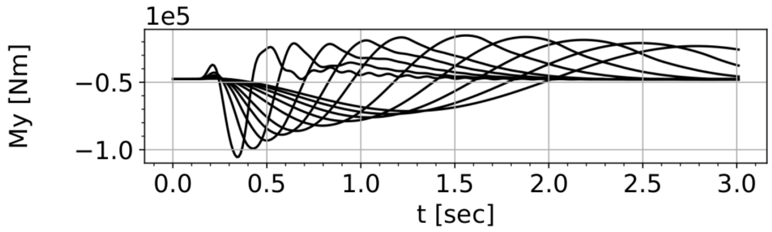

(a) Wing root.

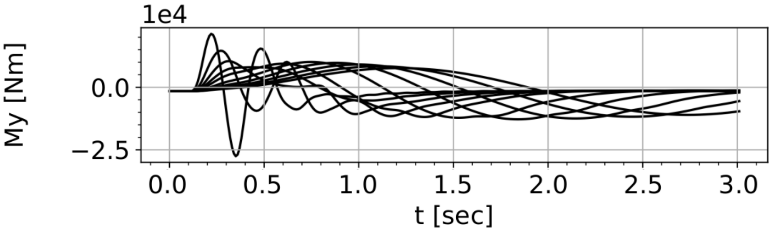

(b) Wing kink.

Figure 5.3.9: Torsional moment M_y over time for different gust gradients.

peak was then arising from a gust with a gust gradient between H = 37 m and H = 51 m. This means the empirical predicted gust gradient value of H = 44 m falls in this range. This goes to show that the unexpected gust load results obtained are justified by this gust and short period coupling that happens for gust profiles with small gust gradients.

5.4 Flutter Check

In the aerospace industry, ensuring the safety and structural integrity of aircraft is paramount. Flutter analysis is a critical component of this process. Flutter occurs when aerodynamic forces interact with the structural dynamics of an aircraft, leading to potentially dangerous oscillations. These oscillations can rapidly escalate, causing structural fatigue and even failure if left unchecked. By conducting flutter analysis, it is possible to identify potential flutter conditions, assess their impact on the aircraft's structure, and implement necessary design modifications or control measures to mitigate the risk. Ultimately, flutter analysis helps to guarantee the safety and reliability of aircraft during operation.

To conduct the flutter check, either the *Loads Kernel* or *MSC Nastran* SOL145 was used. The flutter calculation was executed at FL000, where Equivalent Airspeed (EAS) is equal to True Airspeed (TAS), and the M3 mass configuration was adopted to align with prior analyses. The pk-method was employed for the flutter check in both instances.

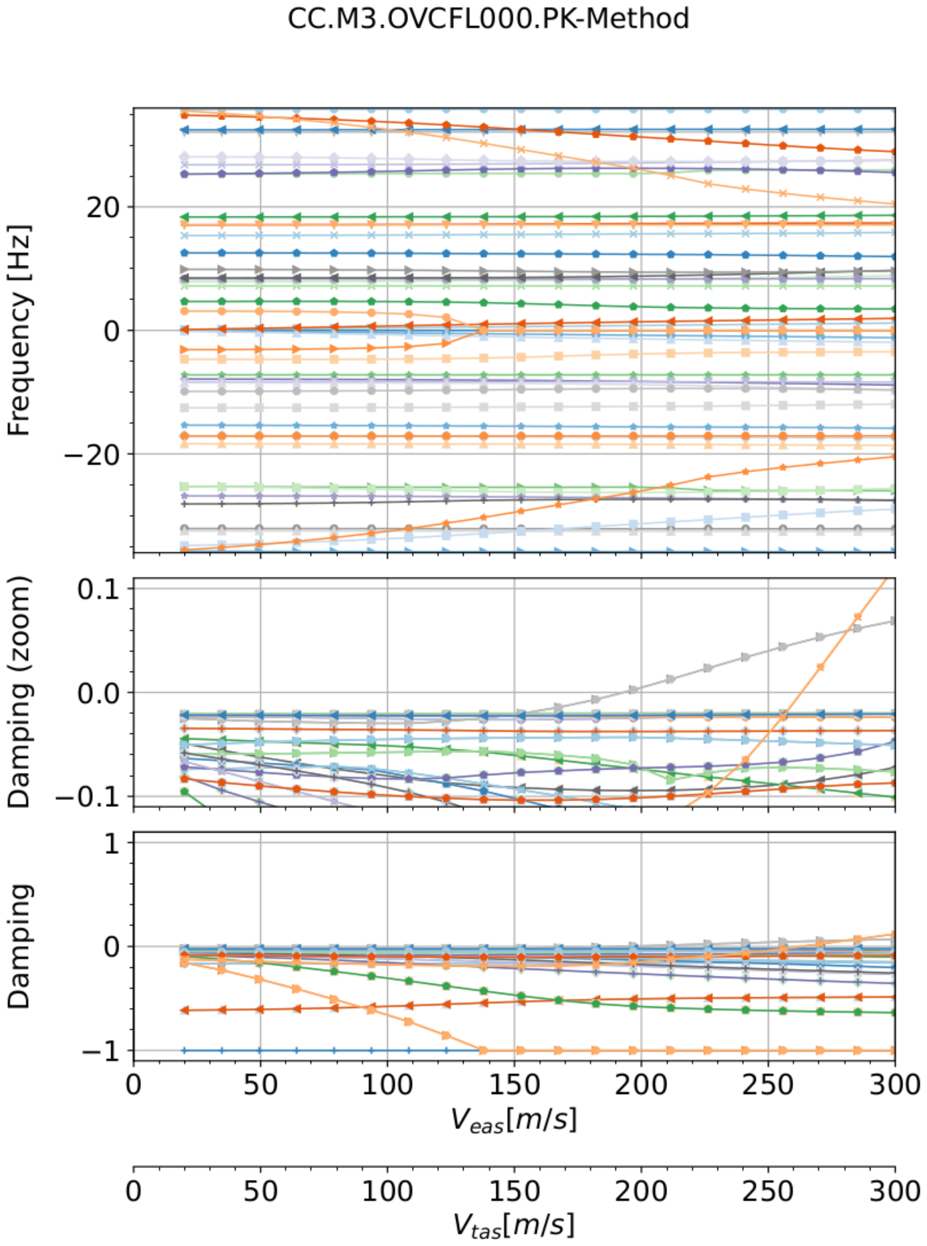

Figure 5.4.1: Flutter results *Loads Kernel*.

Figure 5.4.1 illustrates the results of the flutter check conducted using *Loads Kernel*. The figure comprises two plots: one displaying the frequency of the modes as a function of velocity, and the other depicting the damping of the modes relative to velocity.

In the frequency plot, each eigenmode's frequency and its variation with velocity are evident. Negative frequency values arise due to the nature of solving the eigenvalue problem, yielding conjugate pairs of eigenvalues. Typically, eigenvalues with negative imaginary parts are disregarded, yet *Loads Kernel* retains them, as occasionally some eigenvalues may be lost in the selection process, e.g. when eigenvalues become purely real. In this case, the plot exhibits complete symmetry about the x-axis.

In the damping plot, the evolution of each eigenmode's damping with velocity is portrayed. Initially, at low velocities, all eigenmodes exhibit negative damping, indicating stability. However, at a velocity of 195 m/s, the eigenmode with a frequency of 9.60 Hz becomes unstable, marking the flutter speed $V_{flutter} = 195$ m/s, equivalent to M = 0.569. This mode represents the symmetrical pure torsion mode, maintaining a constant frequency across velocities. Subsequently, at 262 m/s, the mode with a frequency of 36.00 Hz also becomes unstable. This mode corresponds to a high-order symmetrical bending and torsion coupling mode, exhibiting a decrease in frequency from 36 Hz to 23 Hz as instability approaches.

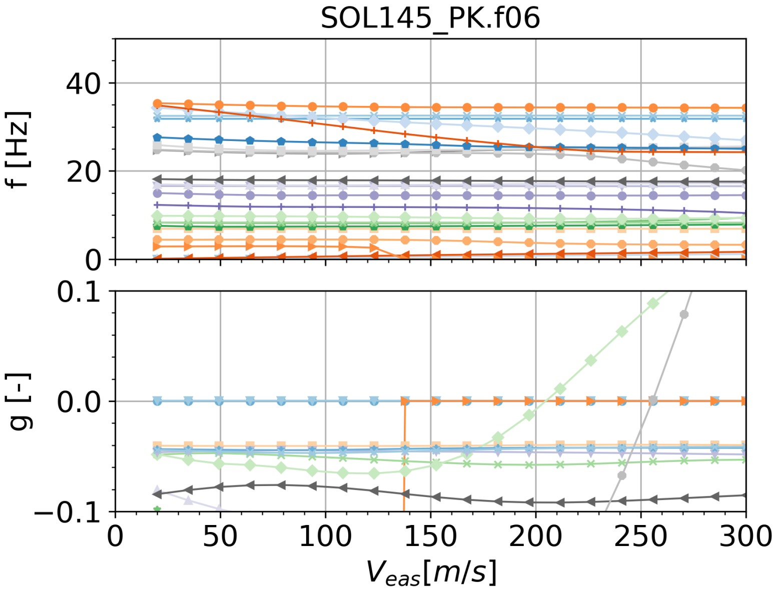

Figure 5.4.2: Flutter results *MSC Nastran*.

Examining the *MSC Nastran* SOL145 results (see Figure 5.4.2), it is evident that at lower velocities, all eigenmodes exhibit negative damping, indicating stability. However, at a velocity of 203 m/s, the eigenmode with a frequency of 9.60 Hz becomes unstable, marking the flutter speed $V_{flutter} = 203$ m/s, equivalent to Ma=0.592. Comparing these findings with those from the *Loads Kernel* results, the first eigenmode to become unstable is the same, although at a slightly higher velocity in the case of *MSC Nastran*. Nevertheless, the results are remarkably consistent.

At 256 m/s, another mode with a frequency of 26.19 Hz becomes unstable. Unlike the mode that became unstable around this velocity in the *Loads Kernel* analysis, this mode corresponds to a different high-order symmetrical bending and torsion coupling mode. In this instance, the frequency of the mode decreases from 26.19 Hz to 23 Hz by the time instability occurs. Thus, both *Loads Kernel* and *MSC Nastran* cases exhibit eigenmodes with a frequency of 23 Hz at the onset of instability, despite their differing initial frequencies.

It's worth noting that both flutter speeds obtained lie outside the flight envelope ($V_{NE} = 119.72$ m/s), yet they remain within the subsonic regime (Ma<0.6), as intended.

Chapter 6

Conclusion and Outlook

The development of the Douglas DC-3 aeroelastic model effectively addresses the critical knowledge gap identified in the Introduction by providing a representative and comprehensive model for demonstration and testing purposes, available as open-source software here. Furthermore, detailed tutorials on the model and the various simulations conducted are available here. This work underscores the pivotal role of aeroelasticity in aircraft design, performance, and flight dynamics and stability. The model meets all requirements, balancing complexity and simplicity, thoroughly testing software features, and capturing aeroelastic phenomena.

The Douglas DC-3 model features a conventional configuration with two engines and control surfaces, including ailerons, elevators, and a rudder. Its wing has a leading-edge sweep angle of $\Lambda_{LE} = 15.5°$, a dihedral angle of $\Gamma = 5°$, an aspect ratio of $AR = 9.2$, and a cambered airfoil. Operating in a subsonic flight regime, the aircraft is easily recognizable and representative, with extensive publicly accessible data. The model exhibits notable wing bending and torsion during level flight, with a clear flutter mechanism coupling bending and torsion modes.

The development process included creating a finite element model using beam elements, aerodynamic models using the Doublet Lattice Method (DLM), and a manually developed mass model. The fuel mass model was created using *ModGen* due to its complexity. Four distinct mass configurations were outlined: operational empty mass (OEM), maximum range (OEM plus maximum fuel capacity), maximum take-off mass (MTOM), and OEM with maximum capacity excluding fuel. The original aircraft model was modified to achieve the desired model by tuning the wing's stiffness properties, redistributing the masses across the wing nodes, and moving the wing LRA forward. The first eigenmode of the final aeroelastic model has an eigenfrequency of 3.17 Hz, outside the expected range due to significant tuning.

Trim case analyses were performed using both *Loads Kernel* and SOL144 in *MSC Nastran* for comparison. Three trim cases at a TAS of 70 m/s, FL000, and Load Factors of n_Z =1, -1, and 2.5 were conducted on both flexible and rigid aircraft configurations. The results from both software matched well, with minor differences arising because *Loads Kernel* uses a modal approach, while SOL 144 in *MSC Nastran* does not. The comparison revealed significant disparities between the rigid and flexible aircraft configurations, with flexibility contributing a detrimental -5.22% to the lift coefficient in horizontal level flight.

To demonstrate *Loads Kernel*'s capabilities, the resulting loads were integrated at designated monitoring stations along the wingspan to derive section loads, using CS-25 as a reference for maneuver selection. In addition to the three trim case maneuvers, two roll maneuvers were added. Critical load cases were identified by constructing two-dimensional load envelopes illustrating significant section load combinations (M_x/M_y load envelope), and one-dimensional envelopes along the wingspan for M_x, M_y, and F_z were plotted.

Additionally, gust loads were studied using the (1-cos) Discrete Gust Model in *Loads Kernel*, with gust profiles selected according to CS-25.341. Load envelopes, similar to the maneuver loads ones were plotted, and forces and moments of different gust profiles were plotted over time. These last plots revealed a coupling between the gusts and one of the longitudinal flight mechanics modes, the short period, due to the model's high static margin.

Finally, a flutter check was conducted to compare both programs. The *Loads Kernel* and *MSC Nastran* SOL145 results matched well, with flutter speeds of 195 m/s and 203 m/s, respectively. In both cases, the eigenmode that became unstable was the symmetrical pure torsion mode, demonstrating the similarity in results obtained from both software.

Future work could focus on a variety of analyses, including investigations into control surface effectiveness, aeroelastic derivatives, longitudinal stability, and continuous turbulence. Furthermore, to validate these results, high-fidelity methods like Computational Fluid Dynamics (CFD) can be employed.

Bibliography

[1] Albano, E. and Rodden, W. “A Doublet-Lattice Method for calculating the lift distribution on oscillating surfaces in subsonic flow”. In: *AIAA Journal* 2.7 (1969), pp. 279–285.

[2] Anderson, R. “Weight Estimation Methods”. Unpublished Notes, Design Branch, Air Force Flight Dynamics Laboratory. Wright-Patterson AFB, Ohio, July 1973.

[3] Assadourian, Arthur and Harper, John A. *Determination of the Flying Qualities of the Douglas DC-3 Airplane*. Report. University of North Texas Libraries, UNT Digital Library, Dec. 1953. URL: `https://digital.library.unt.edu/ark:/67531/metadc56979/` (visited on 02/26/2024).

[4] Bäck, P. and Ringertz, U. T. “Convergence of methods for nonlinear eigenvalue problems”. In: *AIAA Journal* (1997).

[5] Baier, Jan. “Gust Load Prediction on Supersonic Fighter Aircraft using Aerodynamic Panel Methods”. Bachelor Thesis. Göttingen: Deutsches Zentrum für Luft und Raumfahrt - Institute of Aeroelasticity, 2023.

[6] Bisplinghoff, R. L., Ashley, H., and Halfman, R. L. *Aeroelasticity*. Cambridge: Addison-Wesley, 1955.

[7] Bisplinghoff, Raymond L., Ashley, Holt, and Halfman, Robert L. *Aeroelasticity*. Dover Publications, 1955.

[8] Borglund, D. and Eller, D. *Aeroelasticity of Slender Wing Structures in Low-Speed Airflow*. Tech. rep. KTH Engineering Sciences, 2014.

[9] Bunny, Concept. *Douglas DC-3 cutaway drawing in high quality*. Accessed: 28 February 2024. 2019. URL: `https://conceptbunny.com/douglas-dc-3/`.

[10] Buttrill, C., Zeiler, T., and Arbuckle, P. “Nonlinear simulation of a flexible aircraft in maneuvering flight”. In: *Flight Simulation Technologies Conference, Guidance, Navigation, and Control and Co-located Conferences*. 1987. DOI: `10.2514/6.1987-2501`. URL: `https://doi.org/10.2514/6.1987-2501`.

[11] *Certification Specifications and Acceptable Means of Compliance for Large Aeroplanes (CS-25)*. European Union Aviation Safety Agency (EASA). 2007.

[12] Cook, Robert D., Malkus, David S., and Plesha, Michael E. *Concepts and Applications of Finite Element Analysis*. New York: Wiley, 1989.

[13] Donley, P. *Summary of Information Relating to Gust Loads on Airplanes*. Tech. rep. Hampton, Virginia: Langley Research Center, NACA, 1950.

[14] Falkner, V. M. “The Calculation of Aerodynamic Loading on Surfaces of Any Shape”. In: *R&M* 1910 (1943).

[15] Gudmundsson, Snorri. *General Aviation Aircraft Design: Applied Methods and Procedures*. 2nd ed. William Andrew Publishing, 2022. ISBN: 978-0-12-818465-3.

[16] Hedman, S. G. “Vortex Lattice Method for Calculation of Quasi Steady State Loadings on Thin Elastic Wings”. In: *Report* 105 (Oct. 1965).

[17] Heeg, Jeniifers, Chwalowski, Pawel, Kuzmina, Svetlana, and Schuster, David M. “Plans and Example Results for the 2nd AIAA Aeroelastic Prediction Workshop”. In: (Jan. 2015).

[18] Heinze, S. “Aeroelastic Concepts for Flexible Wing Structures”. PhD thesis. KTH, Royal Institute of Technology, 2005.

[19] Hoblit, F. M. *Gust Loads on Aircraft: Concepts and Application*. Reston: American Institute of Aeronautics and Astronautics, 1988.

[20] Klimmek, Thomas. *ModGen User’s Manual*. Version 2023-01-17. 2023.

[21] Klimmek, Thomas. “Parametric Set-Up of a Structural Model for FERMAT Configuration for Aeroelastic and Loads Analysis”. In: *ASDJournal (2014), Vol. 3, No. 2* (2014), pp. 31–49.

[22] Kuzmina, S., Ishmuratov, F., Zichenkov, M., and Chedrik, V. “Integrated numerical and experimental investigations of the active/passive aeroelastic concepts on the European research aeroelastic model Euram”. In: *ASD Journal* 2.2 (2011), pp. 31–51.

[23] *MSC Nastran 2023.1 Quick Reference Guide*. MSC.Software Corporation. 2023.

[24] Pratt, K. G. *A Revised Formula for the Calculation of Gust Loads*. Tech. rep. Technical Note 2964. National Advisory Committee for Aeronautics (NACA), 1953.

[25] QuebecAir Corporation. *QuebecAir DC-3 Manual*. Manual. QuebecAir Corporation. 1957.

[26] Rao, S. S. "Optimization of Airplane Wing Structures under Gust Loads". In: *Computers and Structures* 21.4 (1984), pp. 741–749.

[27] Raymer, Daniel. *Aircraft Design: A Conceptual Approach*. AIAA Education Series. AIAA Education Series, 1996. ISBN: 978-1-56347-281-7.

[28] Reddy, J. N. *An Introduction to the Finite Element Method*. Third. McGraw-Hill, 2006. ISBN: 9780071267618.

[29] Ricci, A., Scotti, A., Cecrdle, J., and Malecek, J. "Active control of three-surface aeroelastic model". In: *Journal of Aircraft* 45.3 (May 2008), pp. 1002–1013.

[30] Rivers, M. B. "NASA Common Research Model: A History and Future Plans". In: *NASA Langley Research Center, Hampton, VA 23681* ().

[31] Schweiger, Johannes, Suleman, Afzal, Kuzmina, Svetlana, and Chedrik, Vasily. "MDO Concepts for an European Research Project on Active Aeroelastic Aircraft". In: (Sept. 2002). DOI: `10.2514/6.2002-5403`.

[32] Spaeth, Andreas. *Aus Alt Mach Neu: Die Legendären Douglas DC-3 Werden Neu Erfunden*. Accessed 29 Feb. 2024. MTU AEROREPORT. 2023. URL: `https://www.aeroreport.de/de/aviation/aus-alt-mach-neu-die-legendaren-douglas-dc-3-werden-neu-erfunden`.

[33] Torenbeek, E. *Synthesis of Subsonic Aircraft Design*. 3rd ed. Delft University Press, 1986.

[34] Voß, Arne. *Loads Kernel User Guide Version 1.04s*. Deutches Zentrum für Luft und Raumfahrt, Institute of Aeroelasticity, Göttingen, 136. Oct. 2020.

[35] Waszak, M., Buttrill, C., and Schmidt, D. *Modeling and Model Simplification of Aeroelastic Vehicles: An Overview*. NASA Technical Memorandum 107691. NASA Langley Research Center, Sept. 1992.

[36] Waszak, M. R. and Schmidt, D. K. "Flight dynamics of aeroelastic vehicles". In: *Journal of Aircraft* 25.6 (June 1988), pp. 563–571. DOI: `10.2514/3.45623`. URL: `https://doi.org/10.2514/3.45623`.

[37] Well, M. J. "A hybrid method for nonlinear equations". In: *Numerical methods for nonlinear algebraic equations* 7 (1970), pp. 87–114. URL: `http://scholar.google.com/scholar?cluster=2809964805047274456&hl=en&oi=scholarr`.

[38] Wikipedia contributors. *Douglas DC-3*. Wikipedia. 2024. URL: `https://en.wikipedia.org/wiki/Douglas_DC-3`.